In vivo imaging of microglia-mediated axonal pruning and modulation by the complement system

Tony K.Y. Lim[1] and Edward S. Ruthazer[1,2,*]

1. Department of Neurology & Neurosurgery, Montreal Neurological Institute-Hospital, McGill University, Montreal, Quebec, H3A 2B4; Canada
2. Lead Contact

*Correspondence: edward.ruthazer@mcgill.ca

Summary

Partial phagocytosis – called trogocytosis – of axons by microglia has been documented in *ex vivo* preparations but has yet to be observed *in vivo*. Fundamental questions regarding the mechanisms that modulate axon trogocytosis as well as its function in neural circuit development remain unanswered. Here we used 2-photon live imaging of the developing *Xenopus laevis* retinotectal circuit to observe axon trogocytosis by microglia *in vivo*. Amphibian regulator of complement activation 3 (aRCA3) was identified as a neuronally expressed, synapse-associated complement inhibitory molecule. Overexpression of aRCA3 enhanced axonal arborization and inhibited trogocytosis, while expression of VAMP2-C3, a complement-enhancing fusion protein tethered to the axon surface, reduced axonal arborization. Depletion of microglia also enhanced axonal arborization and reversed the stereotypical escape behaviors to dark and bright looming stimuli. These findings demonstrate that microglia remodel axon morphology through the complement system and that neurons may control this process through expression of complement inhibitory proteins.

Keywords

Microglia, retinotectal, synapse pruning, trogocytosis, complement, looming stimuli, escape behavior, circuit development, CD46, Xenopus laevis

Introduction

Microglia, the immune cells of the CNS, are vital for the maintenance and development of a healthy brain. Constantly surveilling the brain (Nimmerjahn et al., 2005; Wake et al., 2009), these highly phagocytic cells are thought to contribute to developmental synaptic remodeling by phagocytosing inappropriate or supernumerary synapses, a hypothesis that has derived considerable support from histological and immunohistochemical evidence identifying synaptic components within microglia (Paolicelli et al., 2011; Schafer et al., 2012; Stevens et al., 2007; Tremblay et al., 2010). This hypothesis is further supported by numerous studies demonstrating that microglia depletion leads to exuberant axonal outgrowth (Pont-Lezica et al., 2014; Squarzoni et al., 2014), impaired pruning of excess synapses (Ji et al., 2013; Milinkeviciute et al., 2019) and increased spine density during development (Wallace et al., 2020).

The mechanisms for how microglia shape circuits by engulfing synapses is unclear, and direct evidence of complete elimination of synapses by microglial engulfment remains elusive. Microglia have been documented engaging in trogocytosis, or partial elimination, of axons and presynaptic boutons in *ex vivo* organotypic culture (Weinhard et al., 2018). However, it remains to be seen whether trogocytosis of axons by microglia is a phenomenon that occurs *in vivo*.

Even if we accept the hypothesis that microglia trogocytose the axonal compartment, many questions remain. What impact does partial elimination of presynaptic structures have on circuit remodeling? It is unclear whether this phenomenon is important for circuit connectivity and proper wiring of neurons. Does axonal trogocytosis by microglia affect the morphology of individual axons? While disrupting microglial function enhances axon tract outgrowth (Pont-Lezica et al., 2014; Squarzoni et al., 2014), it is unknown if this result is due to a disruption in microglial trogocytosis, or whether non-phagocytic mechanisms are in play. Is axonal trogocytosis by microglia mechanistically similar to complement-mediated synaptic pruning? There is extensive evidence demonstrating that the complement system regulates synaptic pruning by microglia via the complement protein C3 (Paolicelli et al., 2011; Schafer et al., 2012; Stevens et al., 2007). However, KO mice lacking complement receptor type 3 (CR3), the receptor for activated C3, do not exhibit a deficit in microglial trogocytosis (Weinhard et al., 2018), raising the possibility that microglial-mediated axonal trogocytosis is mechanistically distinct from complement-mediated synaptic pruning.

In this study, we addressed these questions and identified an endogenous, neuronally expressed regulator of microglial trogocytosis. By expressing a pH-stable GFP (pHtdGFP) (Roberts et al., 2016) in retinal ganglion cells (RGCs) of *Xenopus laevis* tadpoles, we observed *in vivo* trogocytosis of RGC axons by microglia in real-time. We then developed an assay to monitor axonal trogocytosis in the population of microglia over a period of 24 h. Microglial depletion enhanced axon arborization and inverted the stereotypical escape behavior to dark and bright looming stimuli. RGC overexpression of amphibian regulator of complement activation 3 (aRCA3) (Oshiumi et al., 2009), a neuronally expressed, synapse-associated, complement inhibitory molecule, homologous to mammalian CD46, enhanced axon arborization and inhibited trogocytosis. Further examining the role of the complement system in regulating axon morphology, we found that expression of a membrane-bound C3 fusion protein in RGCs reduced axon arborization. Our findings provide direct *in vivo* evidence supporting the hypothesis that microglia trogocytose presynaptic axonal compartments, impacting axon arborization and proper wiring during development, through a process mediated by the complement system. Our data support the

68 model that axon trogocytosis and microglial-mediated synaptic pruning are mechanistically similar and
69 are controlled by the complement system. We hypothesize that neurons may exert local control of axon
70 remodeling through the expression of complement regulatory proteins such CD46 and its homologues.

71

Results

Microglia in *Xenopus* larvae resemble mammalian microglia

Microglia in *Xenopus* tadpoles can be labeled with IB4-isolectin conjugated fluorophores for *in vivo* imaging (Fig S1). Like microglia in neonatal mammalian models (Dalmau et al., 1997; Smolders et al., 2017), they are highly mobile (Movie S1A), are morphologically dynamic with ameboid-like and primitive ramified-like morphologies (Movie S1B), and respond to tissue injury (Movie S2).

In developing zebrafish larvae, microglia are primarily localized to the cell body layer of the optic tectum, and are excluded from the tectal neuropil (Svahn et al., 2013). Conversely, microglia in developing mammalian models tend to be found in neuropil regions (Dalmau et al., 1997; Hoshiko et al., 2012; Tremblay et al., 2010). In the *Xenopus laevis* retinotectal circuit, RGC axons project to the neuropil of the contralateral optic tectum, where they synapse on tectal neurons (Fig 1A). To examine whether microglia interact with the tectal neuropil, the neuropil region was labeled by bulk electroporation of RGC neurons with a plasmid encoding pH-stable pHtdGFP. *In vivo* live imaging revealed that, similar to the case in mammals, microglia in developing *Xenopus* associate with both cell bodies and neuropil (Movie S3A). Microglia were observed entering the neuropil region from the cell body layer (Fig 1B and Movie S3B), as well freely moving through the neuropil region (Fig 1C and Movie S3B). Additionally, microglia in the cell body layer extended processes into the neuropil to contact axons, with interactions ranging from minutes to hours in duration (Fig 1D and Movie S3C).

In vivo imaging of RGC neurons reveals microglial trogocytosis of axons and presynaptic structures

We then sought to examine whether microglia cells trogocytose RGC axons. As endosomal organelles are typically acidic (Casey et al., 2010), when performing live imaging of trogocytosis the pH-stablilty of dyes and fluorescent proteins (FP) must be carefully considered (Shinoda et al., 2018). To reduce quenching of FP fluorescence, we utilized pHtdGFP (pKa = 4.8) which is more pH-stable than EGFP (pKa = 6.15) (Roberts et al., 2016). We expressed pHtdGFP in RGC neurons by electroporation, and labeled microglia with Alexa 594-conjugated IB4-isolectin (Fig 1A). 2-photon live imaging revealed occasional increases in microglial green fluorescence following an interaction with a pHtdGFP-labeled axon (Movies S4A and S4B). In one example (Fig 1E), the green fluorescence in the microglial cell increased 3-fold following interaction with a pHtdGFP axon (Fig 1F). The real-time increase in microglial green fluorescence suggests that the microglial cell trogocytosed the pHtdGFP-labeled axon and provides the first direct *in vivo* evidence of presynaptic trogocytosis by microglia.

Increasing the number of pHtdGFP-labeled axons in the optic tectum is expected to lead to more frequent interactions between pHtdGFP-labeled axons and microglia, resulting in greater amounts of green fluorescence within the microglial population, which we could then measure as a proxy of trogocytosis. Based on this principle, we developed an assay to measure trogocytosis of RGC axons in *Xenopus* larvae. At developmental stage 39/40, microglia and RGC neurons were labeled by intraventricular injection of Alexa 594-conjugated IB4-isolectin and by pHtdGFP electroporation respectively (Fig 2A). By two days post-electroporation, axons begin expressing pHtdGFP as they innervate the optic tectum. At 4 d and 5 d post-electroporation, the optic tectum was imaged by 2-photon microscopy. The number of pHtdGFP axons present in the optic tectum was counted and the green fluorescence within the population of microglia was quantified using 3D masking with the IB4-isolectin channel (Fig 2B). To control for the possibility of RGC apoptosis, data was excluded if apoptotic

113 bodies were observed, or if the number of axons decreased from day 4 to day 5. At day 4, there is a
114 weak positive relationship between the number of pHtdGFP-labeled axons in the optic tectum and green
115 fluorescence within microglia (Fig 2C). Even in the absence of pHtdGFP-labeled axons, microglia have a
116 basal level of autofluorescence due to the presence of lipofuscin, bilirubin, and porphyrins which are
117 enriched in myeloid cells (Mitchell et al., 2010). However, when comparing the green fluorescence
118 within microglia on day 4 to day 5, a significant increase in green fluorescence on day 5 was observed if
119 pHtdGFP axons were present within the optic tectum (Fig 2D). Additionally, the change in green
120 fluorescence intensity from day 4 to day 5 is correlated with the number of live pHtdGFP-labeled axons
121 in the optic tectum (Fig 2E), suggesting that microglial cells are accumulating pHtdGFP from intact axons
122 over time. Importantly, the fluorescent label accumulated in microglia was not the result of clearing
123 debris from apoptotic cells, as we were able to follow all pHtdGFP-expressing axons throughout the
124 imaging period.

125 To determine whether microglial trogocytosis of axons included presynaptic components, we
126 generated a synaptophysin-pHtdGFP fusion protein (SYP-pHtdGFP). SYP is a presynaptic vesicle protein
127 (Valtorta et al., 2004), and SYP-FP fusion proteins are commonly used as synaptic vesicle markers
128 (Nakata et al., 1998). Expressing SYP-pHtdGFP in RGC neurons yielded axons with the majority of
129 pHtdGFP concentrated at synaptic puncta (Fig 2F). When SYP-pHtdGFP is used in place of pHtdGFP in the
130 trogocytosis assay, similar results are obtained. A significant increase in microglial green fluorescence is
131 detected on day 5 compared to day 4 (Fig 2G). In addition, a positive correlation between the number of
132 SYP-pHtdGFP expressing axons and the change in microglial green fluorescence was observed (Fig 2H).

133 **Depletion of microglial cells by colony stimulating factor 1 receptor (CSF1R) antagonism enhances RGC**
134 **axon branching and reverses the profile of behavioral responses to dark and bright looming stimuli**

135 To assess the functional roles of microglial trogocytosis, we depleted microglia using PLX5622,
136 an inhibitor of CSF1R, which is a tyrosine kinase receptor essential for microglia survival (Elmore et al.,
137 2014; Erblich et al., 2011). Animals reared in 10 µM PLX5622 had significantly reduced microglia
138 numbers in the optic tectum compared to vehicle treated animals (Fig 3A and 3B). Additionally,
139 morphological analysis of surviving microglia revealed a reduction in the number of processes per
140 microglial cell (Fig 3C).

141 Next, we interrogated the effect of microglial depletion on the morphology of single axons.
142 Axons were followed for several days in control and microglial depleted animals (Fig 3D). Microglial
143 depletion with PLX5622 did not affect axon arbor length (Fig 3E), however a significant increase in axon
144 branch number was observed (Fig 3F), supporting the hypothesis that microglia negatively regulate
145 axonal arborization.

146 We then sought to delineate the functional effects of microglial depletion on the development
147 of the retinotectal circuit. Previous reports in *Xenopus* and in zebrafish have shown that the retinotectal
148 circuit is a vital processing and decision-making center for the visual detection of looming objects (Dong
149 et al., 2009; Khakhalin et al., 2014). Therefore, we developed a free-swimming looming stimulus assay in
150 *Xenopus* tadpoles (Fig 4A) to delineate the functional outcomes of a lack of trogocytosis on RGC axons.
151 In this assay, an exponentially expanding circular looming stimulus is projected onto an opaque screen
152 on the side of a glass tank. The tadpole is contained in a petri dish and the behavioral response to the
153 looming stimulus is recorded by a webcam from above. Either dark looming stimuli or bright looming
154 stimuli were presented to the tadpole (Fig 4B). Custom computer vision tracking software was then used

155 to automatically track the tadpole, collect motor responses, and generate a contrail for analysis of the
156 movement of the tadpole following the onset of the looming stimulus (Fig 4C).

157 Contrails from representative animals in response to dark looming stimuli and bright looming
158 stimuli are shown in Figures 4D and 4E, respectively. In control animals, dark looming stimuli evoked
159 stereotypical defensive escape behavior, whereas microglia-depleted animals were less likely to make
160 such defensive responses to dark looming stimuli (Movies 5A and 5B). In both control and microglia-
161 depleted tadpoles, baseline activity (instantaneous velocity) were observed before the looming stimulus
162 was presented (Fig 4F). After the dark looming stimulus was presented, a peak in instantaneous velocity
163 in control animals was observed at 1.1 ± 0.1 s (mean ± SD, n = 8) post-stimulus. The cumulative distance
164 travelled by the tadpole during a 3 s period after stimulus presentation was significantly greater than the
165 comparable period immediately before presentation for the dark looming stimulus (Fig 4H). This
166 difference was absent in microglia-depleted animals.

167 Contrastingly, bright looming stimuli elicited a very different behavioral response. Bright
168 looming stimuli rarely evoked a defensive escape behavior in control animals, but surprisingly, evoked a
169 robust response in microglia-depleted animals (Movies S6A & S6B). When bright looming stimuli were
170 presented, a peak in instantaneous velocity in microglial depleted animals could be observed 1.9 ± 0.6 s
171 (mean ± SD, n = 8) after the onset of the stimulus presentation (Fig 4G). A comparison of cumulative
172 distance travelled before and after the bright looming stimulus revealed a significant increase in
173 distance travelled following stimulus presentation to microglia-depleted animals, but not control
174 animals (Fig 4J).

175 Tadpole responses to looming stimuli were categorized as exhibiting defensive behavior,
176 absence of defensive behavior or undeterminable (excluded from response rate calculation). The
177 response rate to dark looming stimuli was significantly reduced by microglial-depletion (Fig 4I).
178 Conversely, the response rate to bright looming stimuli was significantly increased by microglial-
179 depletion (Fig 4K). Motor control and kinematics were examined in trials where animals demonstrated
180 escape behavior. No significant changes in escape distance, maximum escape velocity, or initial escape
181 were induced by microglial-depletion (Fig S2).

182 **Bioinformatic identification of a neuronally-expressed membrane-bound complement inhibitory**
183 **molecule, amphibian regulator of complement activation 3 (aRCA3), a homolog of human CD46**

184 Microglial depletion enhanced axonal arborization and perturbed functional development of the
185 retinotectal circuit. As microglia are known to secrete trophic factors and cytokines (Parkhurst et al.,
186 2013; Solek et al., 2018), it is possible non-trogocytosis mediated mechanisms may be at work. In order
187 to discern the role of trogocytosis in modulating axon morphology, a method to inhibit axon
188 trogocytosis without eliminating microglia is required. Complement C3 has been shown to be associated
189 with synapses and is thought to tag synapses for removal by microglial phagocytosis (Schafer et al.,
190 2012; Stevens et al., 2007). It has been postulated that neurons may express complement-inhibitory
191 molecules in order to protect synapses from phagocytosis (Stephan et al., 2012; Stevens et al., 2007). To
192 find such a molecule, we carried out a bioinformatics screen to identify neuronally expressed
193 complement inhibitory proteins.

194 Human complement C3 was queried on the STRING Protein-Protein Association Network (Fig
195 5A), a database which aims to identify physical and functional protein-protein interactions (Szklarczyk et

196 al., 2019). We then refined our search to select for complement inhibitory proteins by focusing on
197 proteins containing CCP (domains abundant in complement control proteins) motifs, which are highly
198 conserved modules abundant in proteins responsible for negative regulation of the complement system
199 (Norman et al., 1991). The top CCP-containing proteins identified by STRING were then queried on the
200 Allen Brain Institute human multiple cortical areas RNA-seq dataset (Allen Institute for Brain Science,
201 2015; Hodge et al., 2019). Of the CCP-containing proteins identified by STRING, only CD46 is highly
202 expressed by CNS neurons (Fig 5B).

203 NCBI protein-protein BLAST was carried out to identify the *Xenopus laevis* homolog of CD46. The
204 *Xenopus laevis* protein with the highest similarity to human CD46 was identified as amphibian Regulator
205 of Complement Activation protein 3 (aRCA3). The Expect value (number of hits expected by chance) of
206 aRCA3 ($3x10^{-41}$) was more than 6 orders of magnitude smaller than the next closest related protein in
207 the *Xenopus laevis* genome. aRCA3 is a protein that is currently uncharacterized in *Xenopus laevis* but
208 has been characterized in *Xenopus tropicalis* as a membrane-associated complement regulatory protein
209 (Oshiumi et al., 2009). The amino acid sequence of aRCA3 was analyzed by the SMART protein domain
210 research tool (Letunic and Bork, 2018; Schultz et al., 1998) to determine conserved modular
211 architecture, and by the Phobius transmembrane topology tool (Käll et al., 2004, 2007) to determine
212 transmembrane topology. aRCA3 has protein architecture similar to that of CD46 – it is a type I
213 transmembrane protein with numerous extracellular CCP domains and a stop-transfer anchor sequence
214 near the C-terminus of the protein (Fig 5C). While the eight CCP domains in Xenopus aRCA3 is twice the
215 number in human CD46, the number of CCP domains of CD46 homologs is known to vary across species.
216 For example, the *Gallus gallus* homolog (Cremp) has 6 CCP domains, while homologs in *Equus caballus*
217 (MCP), *Danio rerio* (rca2.1), and *Coturnix japonica* (MCP-like) each have 5 CCP domains.

218 Next, to investigate whether aRCA3 is endogenously expressed in RGC neurons, we performed
219 fluorescence RNAscope *in situ* hybridization (Wang et al., 2012). Probes against aRCA3, the positive
220 control transcript RNA polymerase II subunit A (polr2a.L), and the bacterial negative control transcript
221 dihydrodipicolinate reductase (DapB) were hybridized on PFA fixed retina sections (Fig 6D). As expected,
222 DapB transcripts were not detected in the retina, whereas the housekeeping transcript polr2a was
223 ubiquitously expressed. aRC3 transcripts on the other hand, were concentrated in the ganglion cell layer
224 (Fig 5E), demonstrating that aRCA3 expression is endogenous to RGC neurons.

225 **aRCA3 associates with synapses, enhances axonal arborization and inhibits microglial trogocytosis**

226 It is unknown whether aRCA3 localizes to the correct cellular compartments to protect axons
227 from complement attack. To examine this, we examined the localization of aRCA3 by tagging it with
228 mCherry, producing an aRCA3-mCherry fusion protein (Fig 6A). This aRCA3-mCherry fusion protein was
229 expressed together with SYP-pHtdGFP, which localizes to synaptic vesicles and synapses (Javaherian and
230 Cline, 2005; Ruthazer et al., 2006). Coexpression of aRCA3-mCherry and SYP-pHtdGFP in RGC axons
231 demonstrates that aRCA3-mCherry and SYP-pHtdGFP colocalize (Fig 6B). Colocalization analysis reveals
232 that mCherry and pHtdGFP fluorescence intensity is highly correlated (Fig 6C), suggesting that aRCA3
233 codistributes to similar subcellular compartments as the presynaptic marker SYP.

234 Next, we examined the effect of aRCA3 overexpression on RGC axon morphology and microglial
235 trogocytosis. RGC neurons were electroporated with pHtdGFP only or both aRCA3 and pHtdGFP, and
236 axon arbors were imaged over several days (Fig 6D). Axon arbor length was significantly increased by
237 overexpression of aRCA3 (Fig 6E), and branch number in RGC axons overexpressing aRCA3 was

238 significantly increased over control axons (Fig 6F). Microglial green fluorescence was also compared
239 between animals where RGC neurons were labeled with pHtdGFP, or with aRCA3 and pHtdGFP. An
240 increase in microglial green fluorescence from day 4 to day 5 was detected in animals which had
241 pHtdGFP-labeled axons present in the optic tectum, but not in animals that had pHtdGFP-labeled axons
242 coexpressing aRCA3 (Fig 6G). Together, these results suggest that aRCA3 inhibits trogocytosis of axons
243 by microglia, which in turn enhances axonal arborization.

244 While CD46 is best known for its ability to deactivate C3b and C4b, CD46 is also capable of
245 signaling through tyrosine kinase activity under certain conditions (Riley-Vargas et al., 2004). This raises
246 the potential caveat that the increased axonal arborization induced by overexpression of aRCA3 may be
247 a result of intracellular signaling. Using a bioinformatic tool, NetPhos3.1 with cutoff scores > 0.6, (Blom
248 et al., 2004), we were unable to predict a tyrosine kinase phosphorylation site on its cytoplasmic region.
249 Nonetheless, it is possible that aRCA3 may be exerting some of its effects through an intracellular
250 signaling pathway. In order to provide further functional validation that the complement system affects
251 axonal arborization, we examined the effects of enhancing complement activity on axon morphology.

252 **Expression of a membrane-tethered Complement C3 fusion protein reduces RGC axon size and**
253 **branching**

254 If aRCA3 is producing its effects on axon morphology through its complement regulatory
255 activity, it stands to reason that enhancing complement activity on single axons should produce effects
256 opposite to that of aRCA3. To explore this possibility, we designed an axon surface-localized C3 fusion
257 protein to enhance complement activity on individual axons (Fig 7A). Synaptobrevin, also known as
258 vesicle-associated membrane protein 2 (VAMP2), is concentrated in synaptic vesicles, though a
259 significant fraction of VAMP2 is also present on the axon surface (Ahmari et al., 2000; Sankaranarayanan
260 and Ryan, 2000). We cloned *Xenopus laevis* complement C3, and fused it to the extracellularly facing C-
261 terminus of *Xenopus laevis* VAMP2. Thus, expression of this VAMP2-C3 construct in RGC neurons results
262 in axons tagged with extracellular membrane-bound complement C3.

263 VAMP2-C3 was co-expressed with pHtdGFP in RGC neurons, and axons were monitored over
264 several days (Fig 7B). To control for the possibility that VAMP2 overexpression may affect axon
265 morphology, we also overexpressed VAMP2 in RGC axons. Expression of VAMP2-C3 in RGC neurons
266 significantly reduced axon arbor length and axon branching when compared to control or VAMP2
267 overexpression (Fig 7C and 7D).

268 **<u>Discussion</u>**

269 ***In vivo* evidence of microglial trogocytosis of axons and synapses during healthy development**

270 Previous experiments in *ex vivo* slice culture have shown that microglia trogocytose presynaptic
271 components (Weinhard et al., 2018). Our results add additional support to the hypothesis that microglia
272 actively engulf presynaptic compartments during development. To our knowledge, these are the first
273 experiments to demonstrate direct evidence of axonal and presynaptic trogocytosis by microglia *in vivo*.

274 **Expression of complement inhibitory or complement enhancing molecules in neurons modulates axon**
275 **morphology and trogocytosis by microglia**

276 Complement C3, when activated, exposes a reactive thioester bond that covalently attaches to
277 amine or carbohydrate groups on cell surfaces (Sahu et al., 1994). Microglia express CR3, a receptor for
278 complement C3 (Ling et al., 1990), and binding of CR3 to its ligand induces phagocytosis (Newman et al.,
279 1985). As C3 has been found deposited on synapses during development, it is thought that complement
280 C3 tags synapses for removal by microglia (Stevens et al., 2007). The importance of the C3 pathway in
281 synaptic pruning has generally been studied by disrupting the C3 pathway using C3 KO mice (Stevens et
282 al., 2007), CR3 KO mice (Schafer et al., 2012), or recently, with the exogenous neuronal expression of the
283 complement inhibitory proteins Crry (Werneburg et al., 2020) and CD55 (Wang et al., 2020). Here we
284 demonstrate that enhancing the C3 pathway with a membrane bound VAMP2-C3 fusion protein
285 increases axonal pruning.

286 C3 is known to undergo spontaneous, low-level activation, a phenomenon called C3 tick-over
287 (Pangburn et al., 1981). It is possible that synapses and axon surfaces are under constant probing by C3
288 tick-over, which in turn is detected by constant microglial surveillance and subsequent trogocytosis.
289 Neurons may determine which axon surfaces or synapses should be removed by localized exposure of
290 membrane-bound complement inhibitory molecules. Indeed, it has been hypothesized that neurons
291 express complement inhibitory molecules to protect synapses from phagocytosis (Stephan et al., 2012;
292 Stevens et al., 2007), although the identity of such a molecule in mammals remains elusive.

293 In this study, we characterized *Xenopus laevis* aRCA3, an endogenous, neuronally expressed,
294 synaptic vesicle associated, complement inhibitory molecule which regulates axon morphology and axon
295 trogocytosis by microglia. aRCA3 is the most similar amphibian homolog of human CD46. CD46 is
296 membrane-bound complement inhibitory molecule that cleaves activated complement components C3b
297 and C4b (Barilla-LaBarca et al., 2002). Using the Allen Brain Institute human multiple cortical areas RNA-
298 seq dataset (Allen Institute for Brain Science, 2015), we report that CD46 transcripts are enriched in
299 human neurons. Interestingly, CD46 is known to associate directly with β1-integrins (Lozahic et al.,
300 2000), a type of adhesion molecule that is present on neuronal surfaces (Neugebauer and Reichardt,
301 1991) and enriched in synaptosomes (Chan et al., 2003), suggesting that it too may be localized to axon
302 surfaces and synapses. In our study we have demonstrated that aRCA3 expression inhibits axon
303 trogocytosis by microglia and enhances axonal arborization – we speculate that CD46 may perform
304 similar functions in mammals. Excessive synaptic pruning is thought to underlie schizophrenia (Sellgren
305 CM et al., 2019), and three large-scale genetic susceptibility studies have identified the CD46 gene as a
306 significant Schizophrenia-risk locus (Håvik et al., 2011; Kim et al., 2020; Ripke et al., 2014). Clearly, the
307 role of CD46 in neurodevelopment warrants further study.

308 **Microglia actively suppress exuberant axonal arborization**

309 Disrupting microglial function by depletion causes exuberant axonal innervation in prenatal
310 models (Pont-Lezica et al., 2014; Squarzoni et al., 2014). However, in prenatal models, depleting
311 microglia also increases the number of neural progenitor cells (Cunningham et al., 2013). Therefore, it is
312 unclear whether the exuberant axonal innervation that occurs following microglial depletion is a result
313 of a deficit of microglial-mediated axonal pruning, or whether it is due to an increase in the overall
314 number of axons. In our experiments, we examined the effect of microglial depletion on the morphology
315 of single axons, demonstrating a significant increase in branching when microglia were depleted. Thus,
316 our study supports the model that the increase in axonal innervation resulting from microglial depletion
317 is due to increased arborization of individual axons.

318 The observation that microglial depletion and RGC overexpression of the complement inhibitor
319 aRCA3 enhanced axonal arborization suggests that both phenomena may be acting through a common
320 mechanism. These results support the hypothesis that trogocytosis suppresses both axon branching –
321 possibly through the removal of new branches – and axon growth – possibly through the physical
322 removal of material from the axon. While this explanation is at odds with the observation that microglia-
323 depletion did not increase axon branch size, it is important to note that in the case of aRCA3
324 overexpression, a single axon gains a relative growth advantage over other axons, which is distinct from
325 the case of microglial-depletion were all axons profit from the same increased growth. If all axons are
326 growing larger at the same pace, competitive mechanisms (Gosse et al., 2008; Ruthazer et al., 2003)
327 would be expected to constrain axon arbor sizes.

328 **Microglial trogocytosis of axons contributes to development of the retinotectal circuit in *Xenopus***
329 ***laevis* under healthy conditions**

330 Visually evoked escape behavior is thought to be driven by a feed-forward network (Khakhalin
331 et al., 2014). In the retina, photoreceptors act on bipolar cells which in turn act on RGCs. Some RGCs are
332 tuned to detect looming (Dunn et al., 2016; Münch et al., 2009), and the population of RGCs that
333 respond to dark looming stimuli are distinct from the population of RGCs that respond to bright looming
334 stimuli (Temizer et al., 2015). Additionally, these distinct RGC populations project to different
335 arborization fields of the optic tectum (Robles et al., 2014; Temizer et al., 2015) where looming
336 computation and behavioral decision making is executed (Barker and Baier, 2015; Fotowat and
337 Gabbiani, 2011). In highly predated animals such as crabs, zebrafish and mice (Oliva et al., 2007; Temizer
338 et al., 2015; Yilmaz and Meister, 2013), dark looming stimuli – which signal imminent threat such as an
339 oncoming object or predator – reliably induce escape responses, whereas bright looming stimuli – which
340 may occur as the animal exits a tunnel or traverses its environment – are less effective.

341 Microglia depletion does not appear to alter motor functionality, suggesting that the hindbrain
342 and motor circuitry are less disrupted by microglia depletion. Instead, the effects of microglia depletion
343 on looming-evoked escape behavior must be occurring further upstream at the retina, the optic tectum
344 or at the projections from the tectal neurons to the hindbrain. As microglia depletion induces exuberant
345 RGC axonal arborization, one possible explanation for why microglia depletion disrupts defensive
346 behavior to dark looming stimuli is that the dark looming sensitive RGC axons are not able to effectively
347 wire with their tectal neuron counterparts which classify threatening visual stimuli due to a disruption in
348 axonal pruning. When microglia are depleted, axons form more errant connections, and dark looming
349 sensitive RGC axons may instead wire together with tectal neurons which are not associated with threat
350 classification, reducing the probability that dark looming stimuli elicit escape responses. We predict that
351 the reverse is true for bright looming sensitive RGC axons, whereby microglia depletion results in
352 increased likelihood of errant wiring between bright looming RGC axons and tectal neurons that classify
353 threatening visual stimuli, leading to enhancement of escape behavior to bright looming stimuli.

354 **Synaptic pruning and trogocytosis are two sides of the same coin: Axonal pruning**

355 Classically, synaptic pruning has been described as the engulfment and elimination of synapses,
356 a phenomenon dependent on the complement pathway (Paolicelli et al., 2011; Perry and O'Connor,
357 2008; Schafer et al., 2012; Stevens et al., 2007). Surprisingly, no deficit in microglial trogocytosis has
358 been observed in CR3 KO mice (Weinhard et al., 2018). One possible interpretation for this result is that
359 synaptic pruning and trogocytosis are different phenomena mediated by different mechanisms.

However, our study suggests that complement-mediated synaptic pruning and trogocytosis, are mechanistically similar. We find that both axonal trogocytosis and axonal arborization are influenced by the complement system. Our findings support the model that microglia trogocytose presynaptic structures and that this in turn is associated with axonal pruning – the loss of unwanted synapses through a reduction in axon arbor size and branching (Riccomagno and Kolodkin, 2015). Finally, our data supports the hypothesis that neurons control microglial-mediated circuit remodeling through the expression of endogenous membrane bound complement inhibitory molecules to regulate microglial trogocytosis.

Acknowledgments

We thank Dr Wayne Sossin, Dr Jean-Francois Cloutier and the MNI Microscopy Core Facility for sharing access to equipment. We also thank Philip Kesner and Anne Schohl for technical advice, Dr Larissa Ferguson for technical assistance, and all members of the Ruthazer lab for helpful discussions. The pFA6a-pHtdGFP plasmid was generously provided by Dr Joerg Stelling. PLX5622 was kindly provided by Plexxikon, Inc. T.K.L. was supported by the CIHR Postdoctoral Fellowship and the McGill Faculty of Medicine McLaughlin Postdoctoral Fellowship. This work was supported by grants to E.S.R. from FRQS and CIHR.

Author Contributions

Conceptualization, E.S.R. and T.K.L.; Methodology, T.K.L. and E.S.R.; Software, T.K.L.; Formal Analysis, T.K.L. and E.S.R; Investigation, T.K.L.; Writing – Original Draft, T.K.L.; Writing – Review and Editing, E.S.R.; Visualization, T.K.L. and E.S.R.; Resources, E.S.R.; Funding Acquisition, E.S.R.; Supervision, E.S.R.

Declaration of Interests

The authors declare no competing interests.

384 **FIGURES**

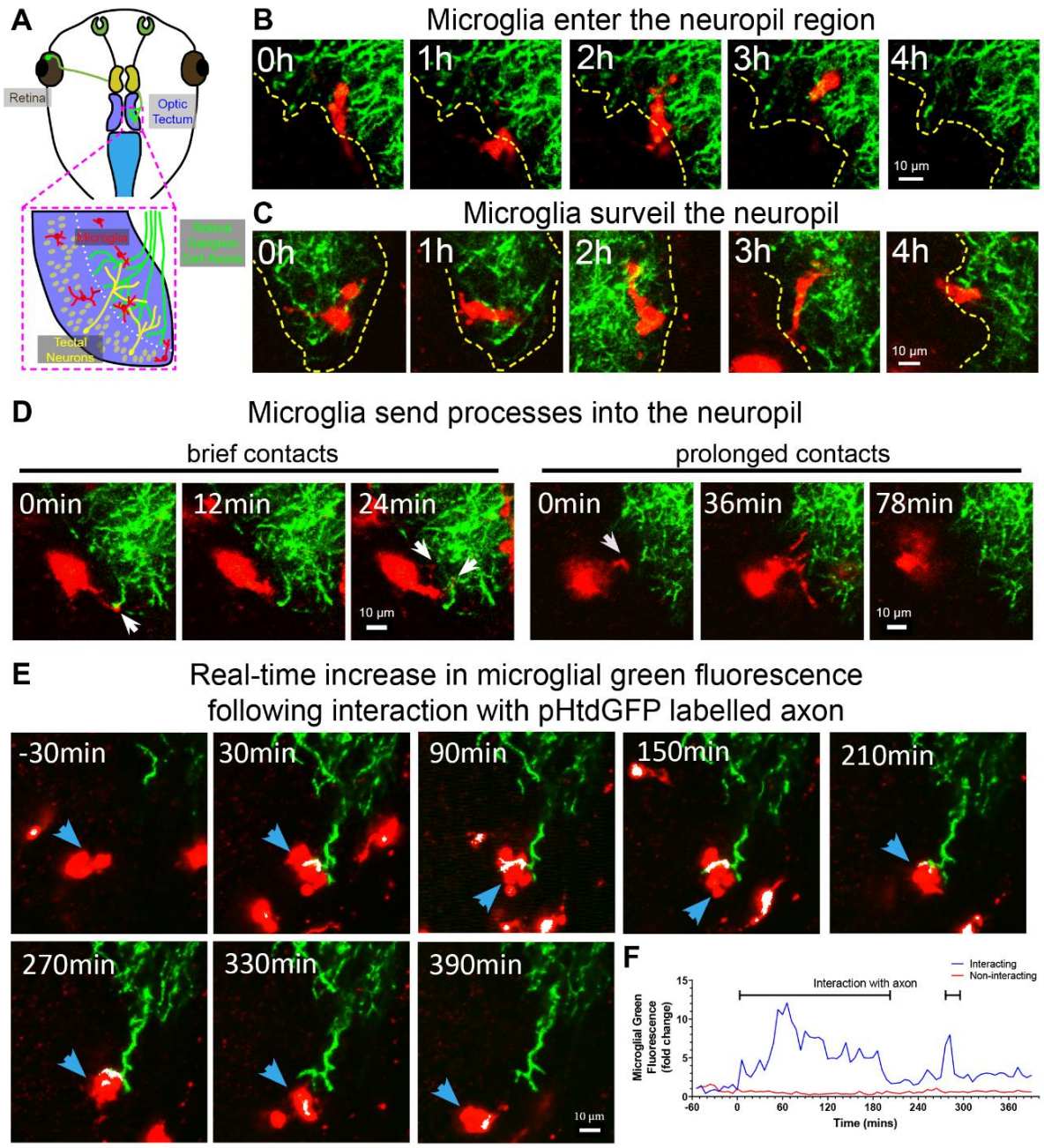

385

386 **Figure 1. Microglia surveil the tectal neuropil, contact RGC axons, and increase in green fluorescence**
387 **following an interaction with pHtdGFP labeled axons in real-time**

388 (A) A diagram of the developing Xenopus laevis retinotectal circuit.

389 (B) The yellow dotted line denotes the border of the cell body layer and the neuropil region. Microglia
390 (red) can be observed migrating into the neuropil region from the cell body layer. A single registered
391 optical section is shown.

392 (C) Microglia surveil the neuropil. A microglial cell is followed over time as it traversed different depths
393 in the tectum.

394 (D) Microglia extend processes into the neuropil. Contact duration varied between minutes and hours.

395 (E) A microglial cell (blue arrow) which interacts with a pHtdGFP labeled RGC axon increases in green
396 fluorescence in real-time. The colocalization of green and red is colorized as white.

397 (F) Quantification of the example shown in Fig 1B. The fluorescence change within an interacting
398 microglial cell (blue), and a non-interacting microglial cell not present in the field (red), is plotted over
399 time.

400

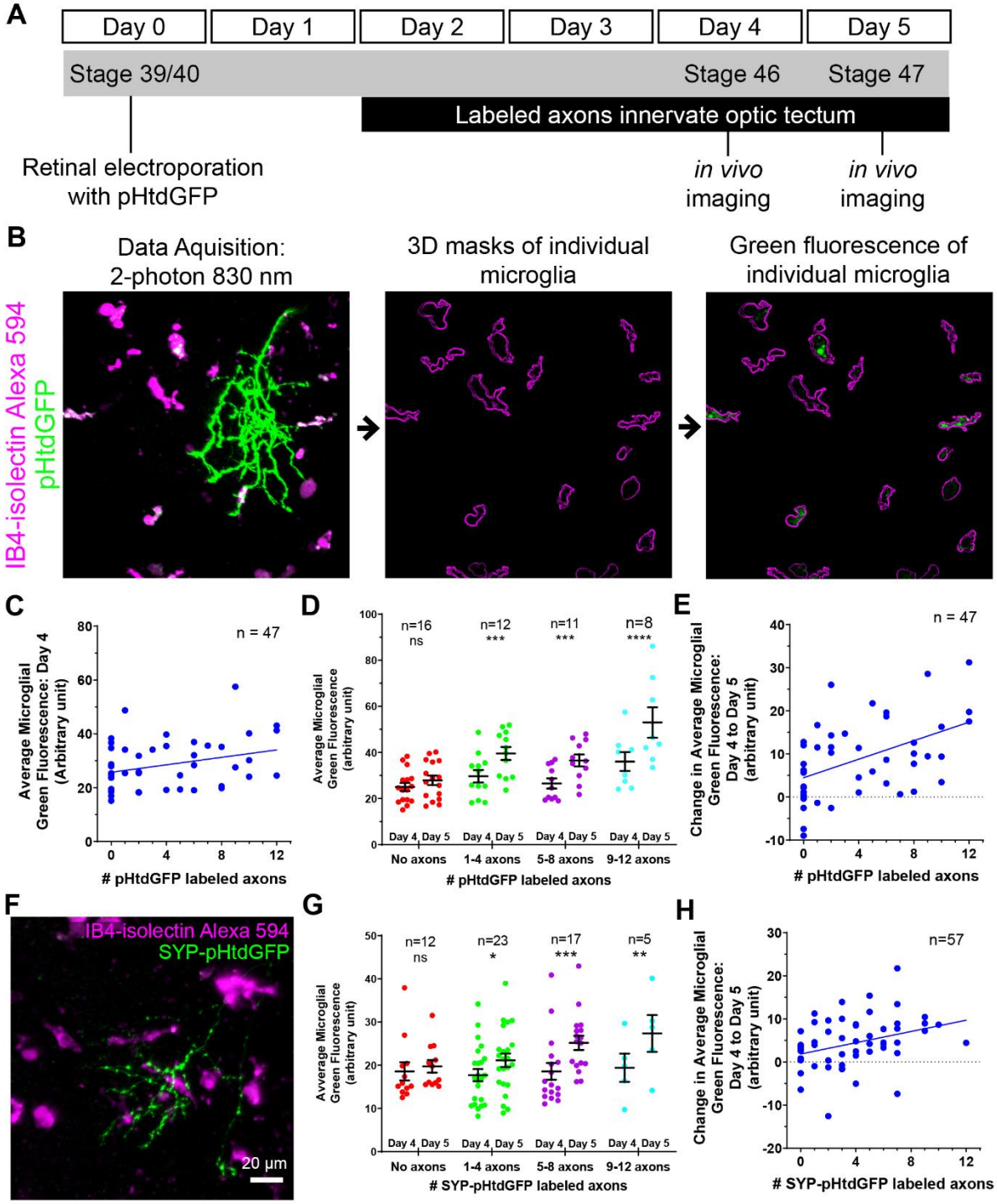

Figure 2. Microglia accumulate green fluorescence from axons expressing pHtdGFP or SYP-pHtdGFP

(A) Timeline of trogocytosis assay.

(B) pHtdGFP-labeled axons (green) were imaged concurrently with microglia (magenta). 3D microglia ROIs were automatically generated (magenta outlines). The average microglial green fluorescence

density per animal was calculated from the population of microglia sampled in the z-stack.
(C) Microglial green fluorescence is weakly correlated to the number of pHtdGFP labeled axons in the optic tectum on day 4. $R^2 = 0.09$, $p = 0.038$.
(D) Microglial green fluorescence is increased on day 5 compared to the previous day when pHtdGFP labeled axons are present. 2-way RM ANOVA interaction $F(3,43) = 6.14$, $p = 0.0014$. Sidak's multiple comparison test ***$p < 0.001$, ****$p < 0.0001$.
(E) The change in microglial green fluorescence from day 4 to day 5 is correlated with the number of pHtdGFP axons. $R^2 = 0.23$, $p = 0.0006$.
(F) A SYP-pHtdGFP fusion protein localizes pHtdGFP to presynaptic puncta.
(G) Microglial green fluorescence is increased on day 5 compared to the previous day when SYP-pHtdGFP labeled axons are present. 2-way RM ANOVA interaction $F(2,49) = 3.33$, $p = 0.044$. Sidak's multiple comparison test *$p < 0.05$, ****$p < 0.0001$.
(H) The change in microglial green fluorescence from day 4 to day 5 is correlated to the number of SYP-pHtdGFP axons. $R^2 = 0.12$, $p = 0.009$.

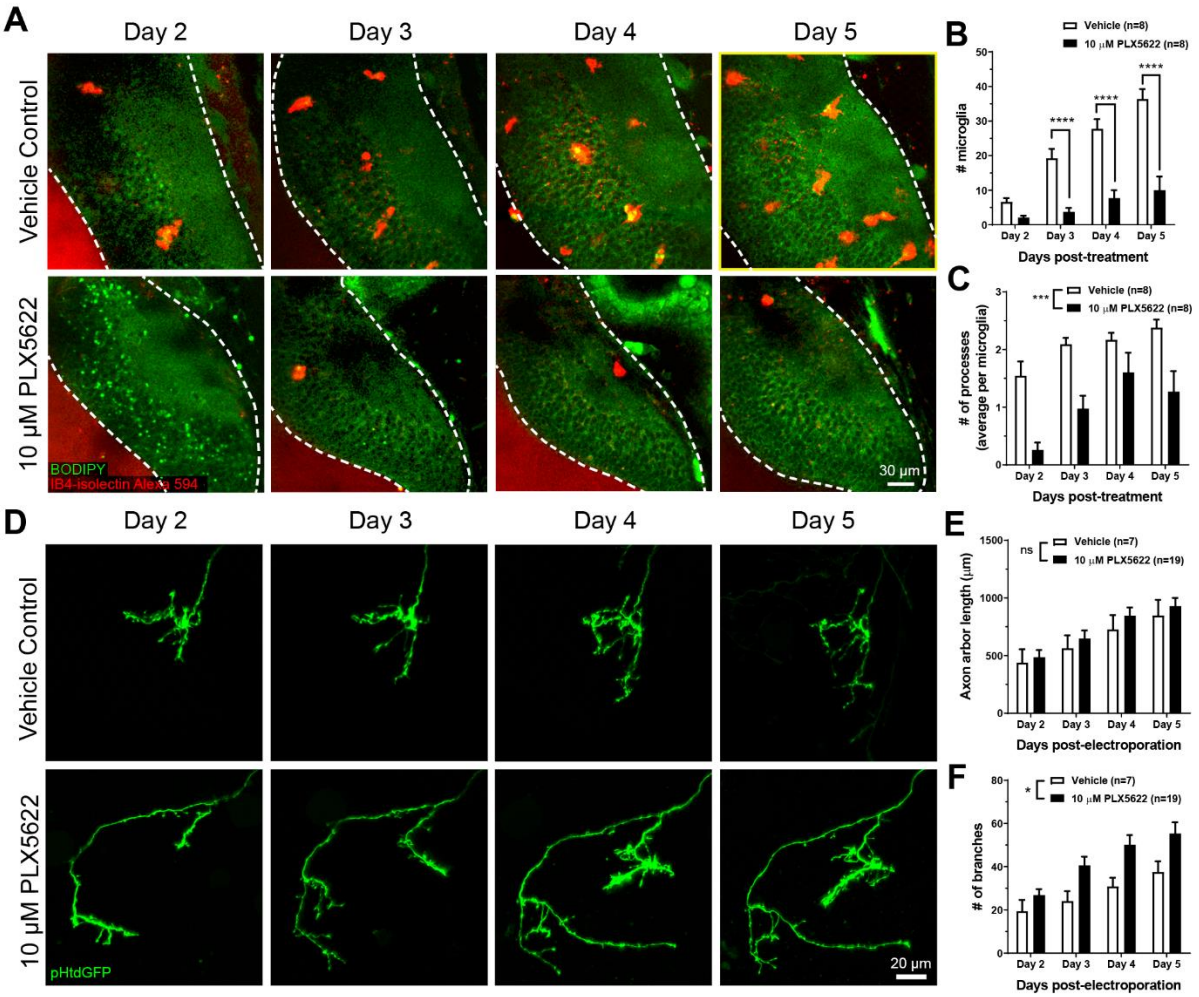

Figure 3. CSF1R antagonism depletes microglia from the optic tectum and increases axon branch number

(A) Animals were treated with vehicle or 10 μM PLX5622. Brain structures and microglia were labeled using CellTracker Green BODIPY (green) and IB4-isolectin (red), respectively. The white dotted line denotes the border of the optic tectum. Single optical sections are shown.
(B) PLX5622 depletes microglia in the optic tectum. Mixed-effects REML model interaction $F(3,39) = 14.23$, $p < 0.0001$. Sidak's multiple comparison post-hoc test **** $p < 0.0001$.
(C) PLX5622 reduces the number of processes per microglia. Mixed-effects REML model main effect $F(1,14)=18.42$, *** $p < 0.001$.
(D) Monitoring of RGC axons in vehicle control and PLX5622 treated animals.
(E) PLX5622 did not affect axon arbor lengths. 2-way RM ANOVA main effect $F(1,24)=0.4141$, $p = 0.53$.
(F) PLX5622 increased axon branch number. 2-way RM ANOVA main effect $F(1,24)=5.581$, $p = 0.027$.

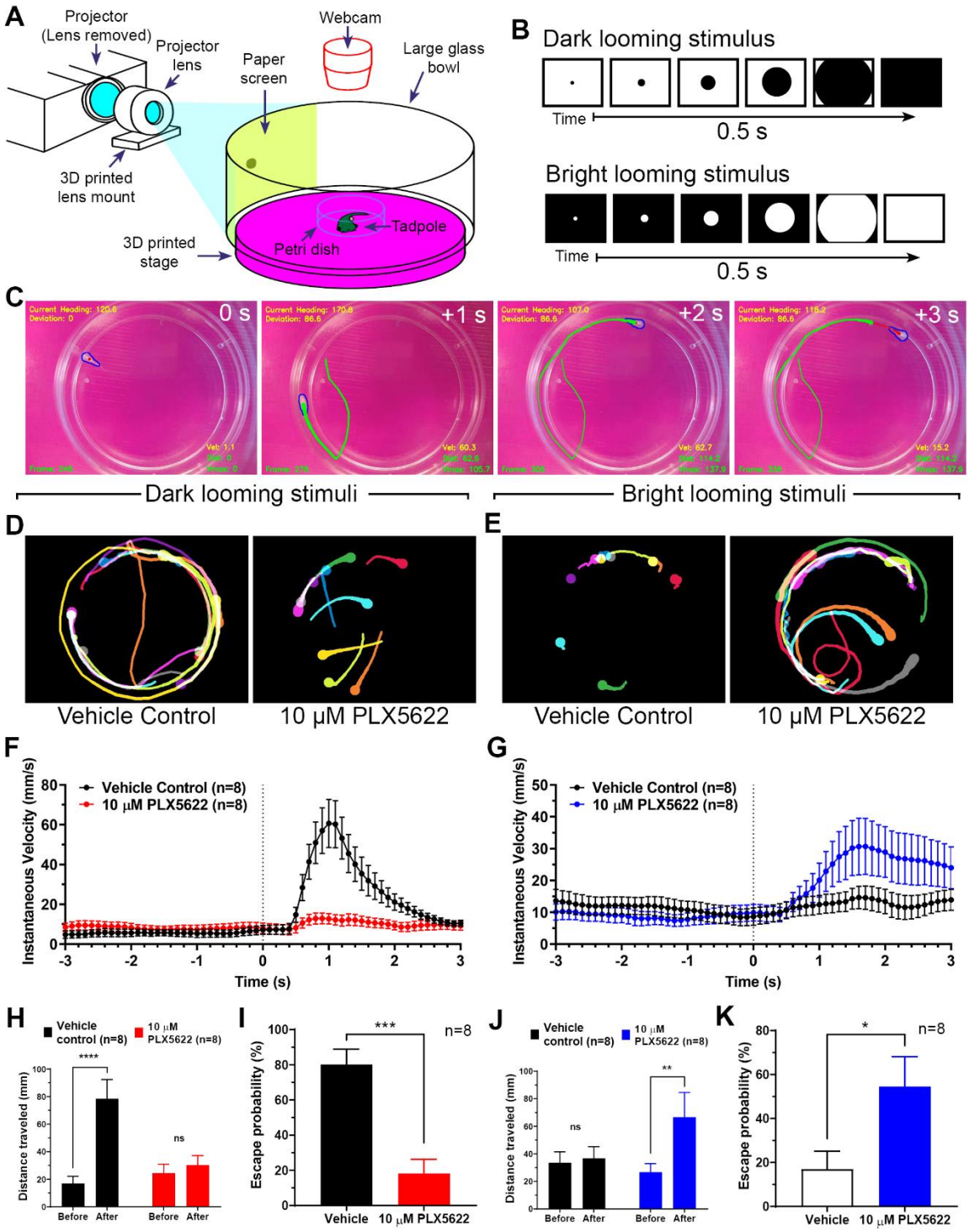

Figure 4. Microglial depletion reverses the expected behavioral response to both dark and bright looming stimuli

(A) Schematic of a looming behavioral task to assess vision and motor responses in *Xenopus laevis* larvae. Stage 47 animals were placed in a petri dish and presented looming stimuli while free-swimming

escape responses were recorded.
(B) Exponentially expanding dark and bright circles were presented as looming stimuli.
(C) Representative response to dark looming stimulus (presented at 0 s) in a vehicle treated animal. Escape contrail (green line), velocity, escape distance, and initial escape angle were quantified.
(D) Representative contrails of the escape responses to dark looming stimuli in 10 trials in a single animal. Characteristic large, exaggerated defensive escape behavior were not observed in the microglia depleted animal.
(E) Representative contrails to bright looming stimuli. Defensive escape behavior was observed in the microglia depleted animal but not in the control animal.
(F) The instantaneous velocity per animal is plotted against time. After the dark looming stimulus was presented (0 s), vehicle treated animals (black) increase in velocity, whereas microglia-depleted animals (red) do not. $n = 8$.
(G) After the bright looming stimulus was presented (0 s), microglia-depleted animals (blue) increase in velocity, whereas vehicle treated animals (white) do not. $n = 8$.
(H) Presentation of dark looming stimuli increased distance traveled in vehicle treated animals (black) but not microglia-depleted animals (red). 2-way RM ANOVA interaction $F(1,14) = 15.82$, $p = 0.0014$. Sidak's multiple comparisons test ****$p < 0.0001$.
(I) Microglia depletion reduced the response rate to dark looming stimuli. Unpaired t-test *** $p < 0.001$, $n = 8$ per group.
(J) Presentation of bright looming stimuli increased distance traveled in microglia-depleted animals (blue) but not vehicle treated animals (white). 2-way RM ANOVA interaction $F(1,14) = 5.291$, $p = 0.037$. Sidak's multiple comparisons test ** $p < 0.01$.
(K) Microglia depletion increased the response rate to bright looming stimuli. Unpaired t-test * $p = 0.033$, $n = 8$.

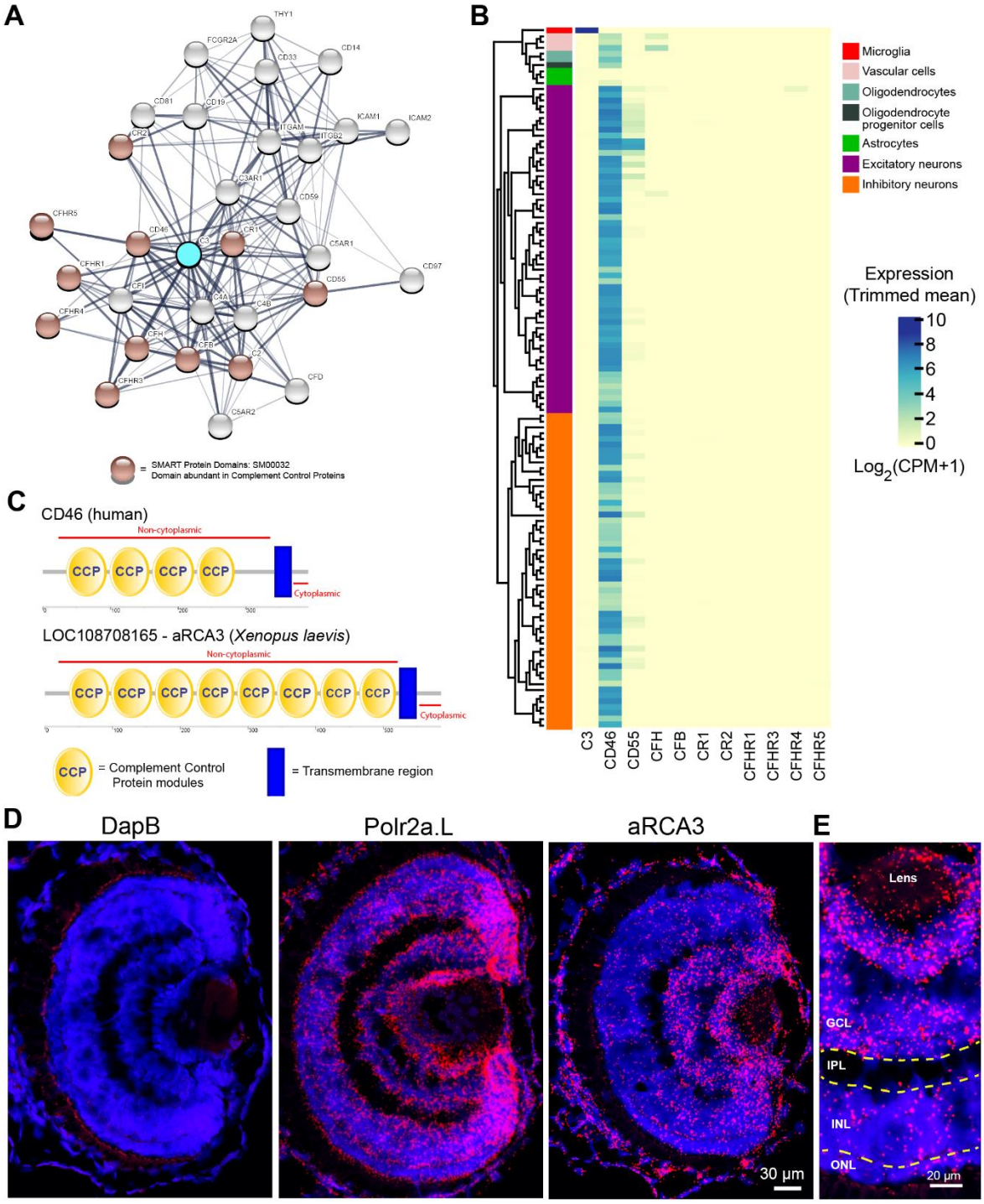

Figure 5. Identification of a neuronally expressed membrane-bound complement inhibitory protein, amphibian regulator of complement activation 3 (aRCA3), the predicted homolog of human CD46

(A) The STRING Protein-Protein Association Network was queried with Complement C3 and the top 30 interaction partners are displayed. Red nodes represent proteins which contain complement control domains that inhibit complement activity. Line thickness indicates the strength of data supporting

473 protein interaction.
474 (B) Complement inhibitory proteins identified by STRING were screened for neuronal expression in the
475 Allen Brain Map human cortical transcriptomics dataset. Cell type taxonomy and hierarchical clustering
476 was determined according to previous analysis (Hodge et al., 2019). Only CD46 is highly expressed by
477 neurons. Heat map color scale denotes log 2 expression levels as represented by trimmed mean (25%-
478 75%). CPM = counts per million.
479 (C) Protein architecture of CD46 and the most similar *Xenopus laevis* homolog (aRCA3) as determined by
480 the SMART protein domain annotation resource and the Phobius transmembrane topology tool. Both
481 human CD46 and *Xenopus laevis* aRCA3 are type I transmembrane proteins, with a non-cytoplasmic
482 region that contains many complement control protein modules, and a transmembrane anchor near the
483 C-terminus.
484 (D) Fluorescent RNAscope *in situ* hybridization on retina sections shows that aRCA3 is endogenously
485 expressed in the retina. Negative control probe DapB was not detected in the retina. Housekeeping gene
486 Polr2a.L was expressed ubiquitously. aRCA3 is expressed in the retina and enriched in specific retinal
487 layers.
488 (E) aRCA3 is highly expressed in the GCL, and is present at lower levels in the INL and ONL. GCL =
489 Ganglion Cell Layer; IPL = Inner Plexiform Layer; INL = Inner Nuclear Layer; ONL = Outer Nuclear Layer

490

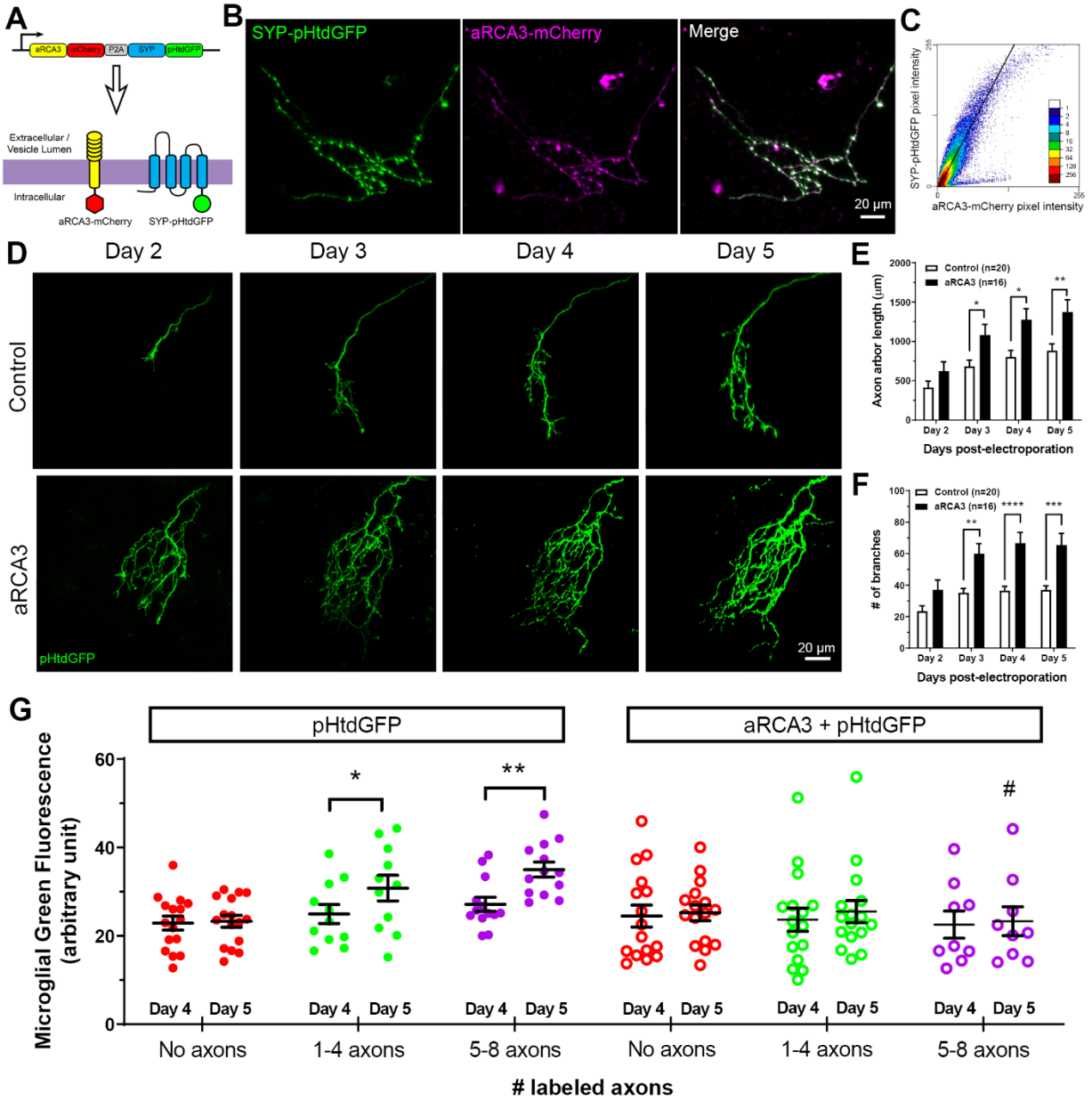

Figure 6. aRCA3 colocalizes with synaptophysin and RGC overexpression of aRCA3 increases axon arbor size and branch number and inhibits microglial trogocytosis

(A) An aRCA3-mCherry fusion protein was co-expressed with SYP-pHtdGFP using a bicistronic P2A plasmid vector.
(B) Representative RGC axon expressing aRCA3-mCherry and SYP-pHtdGFP. SYP-pHtdGFP is concentrated at synaptic puncta. aRCA3-mCherry colocalizes with SYP-pHtdGFP.
(C) Colocalization analysis of the axon shown in B. Scatterplot of pixel intensities demonstrates a high degree of association between aRCA3-mCherry and SYP-pHtdGFP. After applying Costes threshold, Pearson's correlation coefficient = 0.90.
(D) Control and aRCA3 expressing RGC axons imaged over several days.
(E) aRCA3 overexpression increased axon arbor length. 2-way RM ANOVA interaction $F(3,102) = 5.43$, $p =$

503 0.0017. Sidak's multiple comparison test * $p < 0.05$, ** $p < 0.01$.
504 (F) aRCA3 overexpression increased axon branch number. 2-way RM ANOVA interaction $F(3,102) = 4.73$,
505 $p = 0.0039$. Sidak's multiple comparison test ** $p < 0.01$, *** $p < 0.001$, **** $p < 0.0001$.
506 (G) The increase in microglial green fluorescence on day 5 compared to the previous day when pHtdGFP
507 labeled axons are present is inhibited by the overexpression of aRCA3. 3-way RM ANOVA group x time
508 interaction $F(1,75) = 5.15$, $p = 0.026$. False discovery rate for posthoc tests was set to 0.05 and selected
509 significant comparisons are shown. Comparing across timepoints: * $q < 0.05$, ** $q < 0.01$. Comparing
510 across treatment: # $q < 0.05$.

511

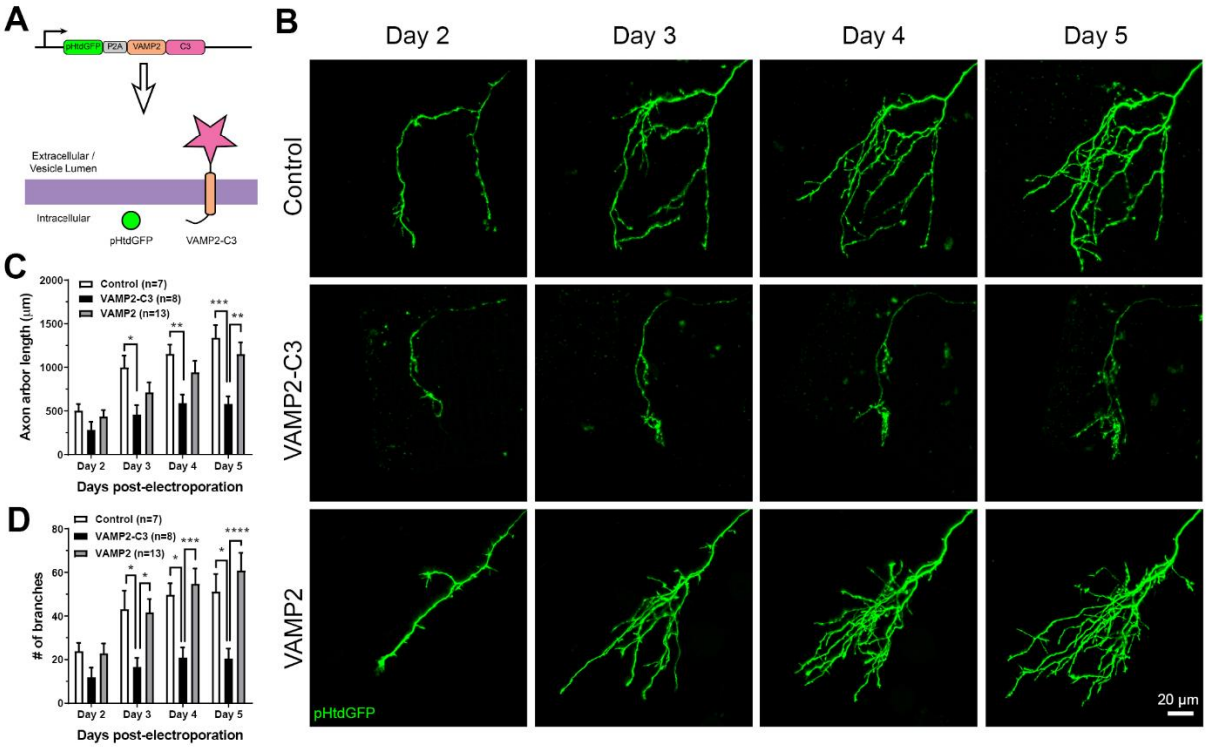

Figure 7. Expressing VAMP2-C3 fusion protein in RGC neurons reduces axon arbor size and branch number

(A) Complement C3 was fused to the N-terminus of VAMP2 to create a complement enhancing molecule which is targeted to the axon surface and synapses. It is expressed together with pHtdGFP in a bicistronic P2A self-cleaving peptide construct.
(B) Axons from control, VAMP2-C3 expressing, and VAMP2 overexpresssing RGC neurons were imaged over several days.
(C) Expression of VAMP2-C3 reduced RGC axon arbor length compared to control and VAMP2 overexpression. 2-way RM ANOVA interaction $F(6,75)=3.48$, $p = 0.0044$. Sidak's multiple comparison test * $p < 0.05$, ** $p < 0.01$, *** $p < 0.001$.
(D) Expression of VAMP2-C3 reduced RGC branch number compared to control and VAMP2 overexpression. 2-way RM ANOVA interaction $F(6,75)=4.15$, $p = 0.0012$. Sidak's multiple comparison test * $p < 0.05$, *** $p < 0.001$, **** $p < 0.0001$.

527

528

529

530 **Supplemental Information**

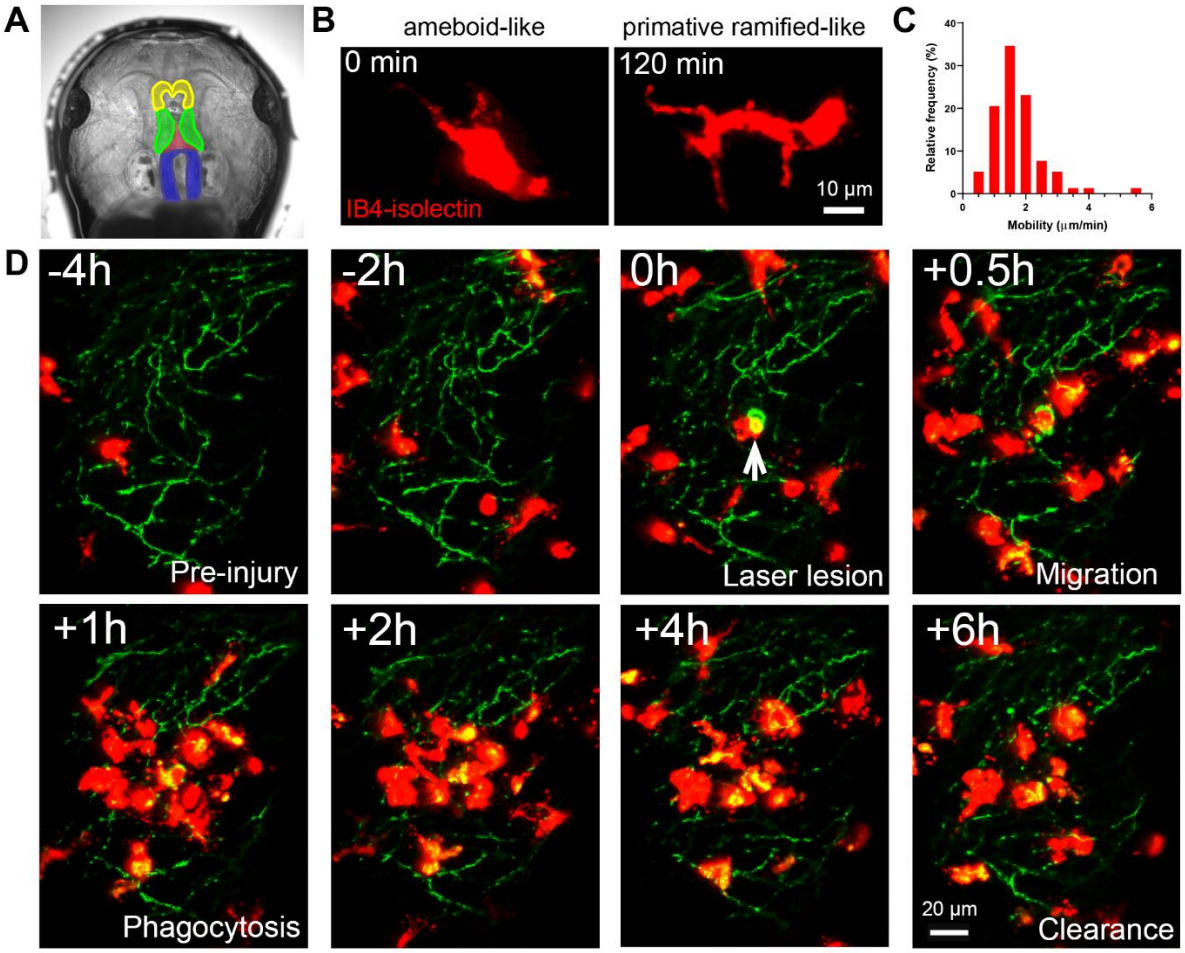

531

532 **Figure S1. IB4-isolectin-conjugated fluorophores label microglial cells in developing *Xenopus laevis***
533 **tadpoles, Related to Figure 1**

534 (A) The tadpole brain colorized for identification (yellow = olfactory bulb and forebrain, green = optic
535 tectum, blue = hindbrain). To label microglia, IB4-isolectin conjugated fluorophores are injected into the
536 3rd ventricle (red).
537 (B) Dynamic cells which have both ameboid-like and primitive ramified-like morphologies are labeled by
538 IB4-isolectin.
539 (C) The distribution in mobility of IB4-isolectin labeled cells under normal conditions. Average velocity is
540 1.75 µm/min.
541 (D) IB4-isolectin labeled cells are shown in red, and eGFP-electroporated RGC axons are shown in green.

542 Laser ablation induced a region of damaged, autofluorescent, tissue. After injury, IB4-isolectin labeled
543 cells mobilize to the injury site and remove the injured tissue by phagocytosis.

544

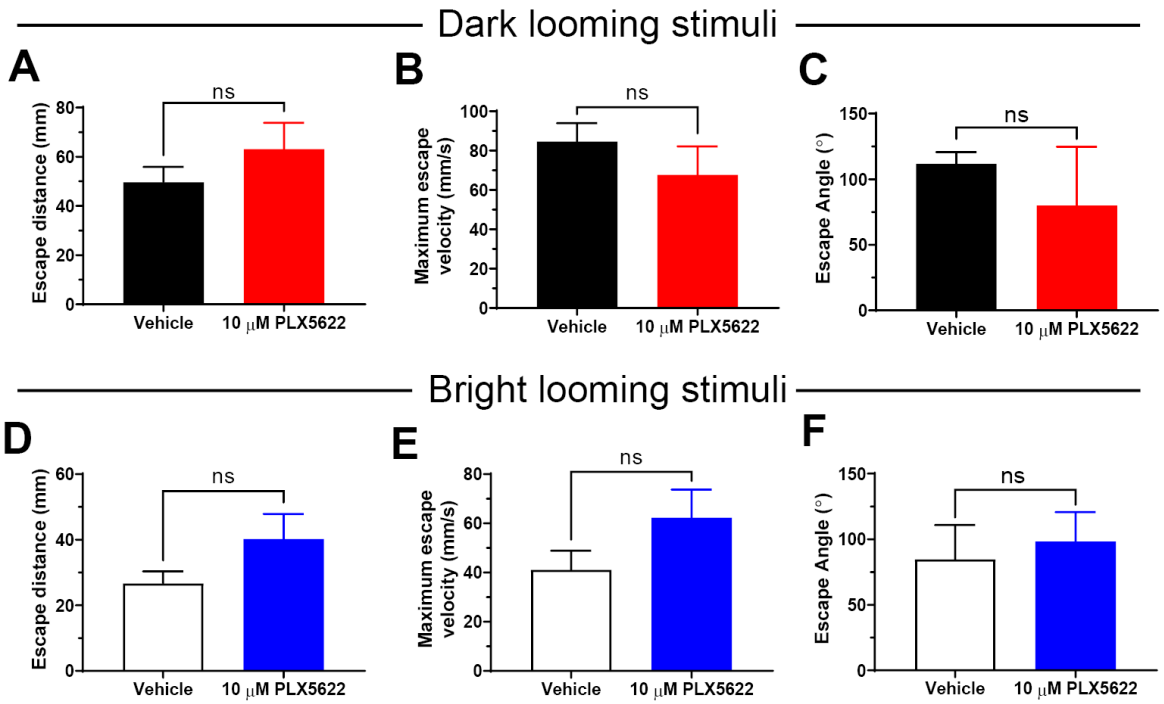

Figure S2. Motor responses to dark and bright looming stimuli are not altered by microglial-depletion with PLX5622, Related to Figure 4

A-F analyze all trials where defensive behavior was exhibited to looming stimuli. Data was collected from 8 animals per group.
(A) Microglial-depletion did not alter escape distance to dark looming stimuli. Unpaired t-test p = 0.27.
(B) Microglial-depletion did not alter maximum escape velocity to dark looming stimuli. Unpaired t-test p = 0.32.
(C) Microglial-depletion did not alter escape angle to dark looming stimuli. Unpaired t-test p = 0.40.
(D) Microglial-depletion did not alter escape distance to bright looming stimuli. Unpaired t-test p = 0.26.
(E) Microglial-depletion did not alter maximum escape velocity to bright looming stimuli. Unpaired t-test p = 0.25.
(F) Microglial-depletion did not alter escape distance to bright looming stimuli. Unpaired t-test p = 0.72.

559 **Movie S1. IB4-isolectin labeled cells in *Xenopus laevis* tadpoles are morphologically dynamic and**
560 **highly mobile, Related to Figure 1**

561 (A) IB4-isolectin cells are highly mobile.
562 (B) IB4-isolectin labeled cells have a dynamic morphology, switching back and forth between ameboid-
563 like and primitive ramified-like morphologies.

564

565 **Movie S2. IB4-isolectin labeled cells respond to tissue injury by mobilization to the injury site and**
566 **phagocytosis of injured tissues, Related to Figure 1**

567

568 **Movie S3. Microglia are associated with the neuropil and surveil the neuropil by entering the neuropil**
569 **and extending processes towards axons from the cell body layer. Related to Figure 1**

570 (A) Microglia associate with the tectal neuropil in *Xenopus laevis*.
571 (B) The neuropil does not exclude microglia. Microglia can mobilize into the neuropil region from the cell
572 body layer and can freely move through the neuropil region.
573 (C) Microglia surveil the tectal neuropil by extending processes towards the neuropil from the cell body
574 layer.

575

576 **Movie S4. *In vivo* real-time trogocytosis in *Xenopus laevis* tadpoles imaged by 2-photon microscopy,**
577 **Related to Figure 1**

578 (A) A microglial cell increases in green fluorescence in real-time after an interaction with a pH-stable GFP
579 labeled axon. The colocalization of green and red is colorized as white.
580 (B) Another example of an increase in green fluorescence within a microglial cell following an interaction
581 with a pH-stable GFP labeled axon. This example is shown in Figure 1E.

582

583 **Movie S5. Representative responses to dark looming stimuli in control and microglia-depleted**
584 **animals, Related to Figure 4**

585 (A) Representative response to dark looming stimuli in a vehicle control animal.
586 (B) Representative response to dark looming stimuli in a microglia-depleted animal.

587

588 **Movie S6. Representative responses to bright looming stimuli in control and microglia-depleted**
589 **animals, Related to Figure 4**

590 (A) Representative response to bright looming stimuli in a vehicle control animal.
591 (B) Representative response to bright looming stimuli in a microglia-depleted animal.

592

STAR Methods

KEY RESOURCES TABLE

REAGENT or	SOURCE	IDENTIFIER
Bacterial and Virus Strains		
DH5α Competent cells	Invitrogen	Cat#18265017
Chemicals, Peptides, and Recombinant Proteins		
Isolectin GS-IB_4 From *Griffonia simplicifolia*, Alexa Fluor 594 Conjugate	ThermoFisher Scientific	Cat#I21413
CellTracker Green BODIPY	ThermoFisher Scientific	Cat#C2102
RNAscope Probe: *Xenopus laevis* polr2a.L	Advanced Cell Diagnostics	Cat#580841
RNAscope Probe: *Xenopus laevis* aRCA3	Advanced Cell Diagnostics	Cat#806291
PLX5622	Plexxikon	N/A
Polyethylene glycol 400	Sigma	SKU#P3265
Poloxamer 407	Sigma	SKU#16758
D-α-Tocopherol polyethylene glycol 1000 succinate	Sigma	SKU#57668
TRIzol Reagent	Invitrogen	Cat#15596-026
Superscript IV First-Strand synthesis system	Invitrogen	Cat#18091050
Phusion High-Fidelity DNA polymerase	ThermoFisher Scientific	Cat#F530S
Sylgard 184 silicone	Paisley	AVDC00184003
Fisher Healthcare Tissue-Plus O.C.T Compound	Fisher Scientific	Cat#23730571
Critical Commercial Assays		
RNAscope Multiplex Fluorescent Reagent Kit v2	Advanced Cell Diagnostics	Cat#323136
Deposited Data		
Allen Brain Map Human Multiple Cortical Areas SMART-seq data set	(Allen Institute for Brain Science, 2015)	portal.brain-map.org/atlases-and-data/rnaseq/human-multiple-cortical-areas-smart-seq
Experimental Models: Organisms/Strains		
Albino *Xenopus laevis* (Xla.NXT-WT:Albino^{NXR})	National Xenopus Resource	NXR_0082
Recombinant DNA		
pCMV eGFP	(Haas et al., 2002)	
pFA6a pH-tdGFP	(Roberts et al., 2016)	Addgene Plasmid #74322
pEF1α pHtdGFP	This paper	
pEF1α SYN-pHtdGFP	This paper	

pEF1α aRC3-P2A-pHtdGFP	This paper	
pEF1α pHtdGFP-P2A-VAMP2	This paper	
pEF1α pHtdGFP-P2A-VAMP2-C3	This paper	
Software and Algorithms		
NCBI protein-protein BLAST	(Altschul et al., 1990)	blast.ncbi.nlm.nih.gov
STRING v11.0 protein-protein association networks	(Szklarczyk et al., 2019)	string-db.org
SMART protein domain annotation resource 8.0	(Letunic and Bork, 2018)	smart.embl-heidelberg.de
Phobius transmembrane topology tool	(Käll et al., 2007)	phobius.sbc.su.se
NetPhos 3.1	(Blom et al., 2004)	www.cbs.dtu.dk/services/NetPhos/
R 4.0.0	(R Core Team, 2018)	www.r-project.org/
RColorBrewer	(Neuwirth, 2014)	cran.r-project.org/web/packages/RColorBrewer/RColorBrewer.pdf
ComplexHeatmap	(Gu et al., 2016)	github.com/jokergoo/ComplexHeatmap
Bioconductor 3.11	(Huber et al., 2015)	bioconductor.org
Serial Cloner 2.6.1	SerialBasics	serialbasics.free.fr/Serial_Cloner.html
Imaris 6	Oxford Instruments	imaris.oxinst.com/products/imaris-for-cell-biologists
Fluoview 5.0	Olympus	www.olympus-lifescience.com/en/support/downloads/
ThorImage LS	Thorlabs	www.thorlabs.com/newgrouppage9.cfm?objectgroup_id=9072#ad-image-0
Leica LAS X	Leica	www.leica-microsystems.com/products/microscope-software/p/leica-las-x-ls/
FIJI ImageJ	(Schindelin et al., 2012)	imagej.net/Fiji
3D Objects Counter plugin	(Bolte and Cordelières, 2006)	imagej.net/3D_Objects_Counter
3D ROI Manager plugin	(Ollion et al., 2013)	imagejdocu.tudor.lu/plugin/stacks/3d_roi_manager/start
TrackMate plugin	(Tinevez et al., 2017)	imagej.net/TrackMate
Descriptor-based series registration plugin	(Preibisch et al., 2010)	imagej.net/SPIM_Registration_Method
3D hybrid median filter plugin	Christopher Philip Mauer and Vytas Bindokas	imagej.nih.gov/ij/plugins/hybrid3dmedian.html
ScatterJ plugin	(Zeitvogel et al., 2016)	savannah.nongnu.org/projects/scatterj
MATLAB	MathWorks	www.mathworks.com/products/matlab.html
CANDLE	(Coupé et al., 2012)	sites.google.com/site/pierrickcoupe/softwares/denoising-for-medical-imaging/multiphoton-filtering

Graphpad Prism 8	GraphPad Software	www.graphpad.com/scientific-software/prism/
Cura 4	Ultimaker	ultimaker.com/software/ultimaker-cura
TinkerCAD	Autodesk	www.tinkercad.com
Psychopy 3.0	(Peirce et al., 2019)	psychopy.org
XenLoom (beta): Looming Stimulus Presentation and Tracking of *Xenopus laevis* tadpoles	This paper	github.com/tonykylim/XenLoom_beta
Other		
Estink 2000 lumens mini LED projector	Amazon.ca	ASIN#B07F7RT9XZ
Custom 3D printed mount for projector lens	This paper	www.thingiverse.com/thing:4335379
Custom 3D printed stage for *Xenopus laevis* behavior	This paper	www.thingiverse.com/thing:4335395
8-inch soda lime 1500 ml culture dish	Carolina	Item#741006
60 mm petri dish	FisherScientific	Cat#FB0875713A
PLA 1.75mm 3D printing filament	iPrint-3D	Transparent purple
Logitech C920 webcam	Logitech	Model# 960-000764
Webcam scissor arm clamp mount	Amazon.ca	ASIN#B01N77YBLU
Anycubic i3 mega 3D printer	Amazon.ca	ASIN#B07NY5T1LJ
Grass SD9 Square Pulse Stimulator	Grass-Telefactor	Model SD9
Custom-built 2-photon microscope	(Ruthazer et al., 2006)	
Thorlabs multiphoton imaging system	Thorlabs	
Ti:Sapphire femtosecond pulsed laser	Spectra-Physics	InSight X3

Lead Contact and Materials Availability

Plasmids generated in this study will be made available upon request. Further information and requests for resources and reagents should be directed to the Lead Contact, Edward Ruthazer (edward.ruthazer@mcgill.ca).

Experimental Model and Subject Details

Xenopus laevis tadpoles

Adult albino African clawed frogs (*Xenopus laevis*) were maintained and bred at 18°C. Female frogs were primed by injection of 50 IU pregnant mare serum gonadotropin. After 3 days, 150 IU of human chorionic gonadotropin (HCG) was injected into the dorsal lymph sacs of male frogs. The primed female

605 frogs were injected with 400 IU into the dorsal lymph sac. The injected male and female frogs were
606 placed in isolated tanks for mating.

607 Eggs were collected the following day and maintained in Modified Barth's Saline with HEPES (MBSH) in
608 an incubator at 20°C with LED illumination set to a 12h/12h day-night cycle and staged according to
609 Nieuwkoop and Faber (NF) developmental stages (Nieuwkoop and Faber, 1994). All experiments were
610 conducted with embryos in the NF stage 35-48 range, according to protocols approved by The Animal
611 Care Committee of the Montreal Neurological Institute and in accordance with Canadian Council on
612 Animal Care guidelines. *Xenopus laevis* sex cannot be determined visually pre-metamorphosis, and thus
613 the sex of experimental animals was unknown.

614 **Method Details**

615 Labelling of microglia

616 Stage 39/40 tadpoles were anesthetized with 0.02% MS-222 in 0.1X MBSH. A micropipette was back
617 filled with 1mg/ml Alexa 594 conjugated IB4-isolectin. Tadpoles received intracerebroventricular (icv)
618 injections to the 3rd ventricle. A minimum of 48 hours was allowed to pass before live imaging studies
619 were commenced to allow for binding and update of IB4-isolectin by microglial cells.

620 Labelling of brain structures

621 Stage 39/40 tadpoles were anesthetized with 0.02% MS-222 in 0.1X MBSH and were then labeled by icv
622 injection of CellTracker Green BODIPY (1 mM in 10% DMSO).

623 Transfection of RGCs by electroporation

624 Electroporation of plasmid DNA into RGC cells was performed as described previously (Ruthazer et al.,
625 2006, 2013a). In brief, stage 39/40 tadpoles were anesthetized with 0.02% MS-222 in 0.1X MBSH. A glass
626 micropipette was back filled with endotoxin free maxi-prep plasmid solution (2-3 µg/µl) and fast green
627 to visualize the injection. The micropipette was advanced into the eye, and DNA solution pressure
628 injected. The micropipette was then withdrawn, and parallel platinum electrodes were placed to bracket
629 the eye.

630 For bulk electroporation of RGCs, a Grass Instruments SD9 electrical stimulator was used to apply 4-6
631 pulses of 2.4 ms duration at 36 V. For single-cell electroporation of RGCs, 4-6 pulses of 1.6 ms duration
632 at 36 V was applied. A 3µF capacitor was placed in parallel to obtain exponential decay current pulses.
633 After 24-48 hours, labeled axons can be observed in the contralateral optic tectum.

634 The following plasmid constructs were used in this study: pCMV-eGFP; pEF1α-pHtdGFP; pEF1α-SYN-
635 pHtdGFP; pEF1α-aRCA3; pEF1α-aRCA3-mCherry-P2A-SYN-pHtdGFP; pEF1α-pHtdGFP-P2A-VAMP2-C3;
636 pEF1α-pHtdGFP-P2A-VAMP2

637 2-photon microscopy live imaging

638 2-photon live imaging of axons and microglia cells was performed as described previously (Ruthazer et
639 al., 2013b). Tadpoles were placed in a Sylgard 184 silicone imaging chamber with their dorsal side facing
640 up and were covered with a #1 thickness glass coverslip. 1 µm interval z-stacks of the optic tectum were
641 collected on a custom-built 2-photon microscope (Olympus BX61WI with Olympus FV300 confocal scan
642 head) outfitted with an Olympus 1.0 NA 60x water-immersion objective, or a Thorlabs multiphoton

643 resonant scanner imaging system outfitted with an Olympus 1.0 NA 20x water-immersion objective.
644 Excitation was produced using a Spectra-Physics InSight3X femtosecond pulsed laser. Images were
645 collected at 512x512 pixels with Fluoview 5.0 or ThorImage LS.

646 *Real-time imaging*
647 Stage 46-48 tadpoles were paralyzed by brief (2-8 min) immersion in freshly thawed 2 mM pancuronium
648 bromide in 0.1X MBSH. Animals were then maintained in 0.1X MBSH for imaging. Z-stacks were
649 collected at 6-minute intervals.

650 *Daily imaging*
651 Once per day, stage 43-47 tadpoles were anesthetized by immersion in 0.02% MS-222. Z-stacks were
652 collected, and animals were returned to 0.1X MBSH rearing solution.

653 *Imaging of microglia and axons*
654 When imaging microglia (Alexa 594 conjugated IB4-isolectin) and RGC axons (eGFP or pHtdGFP)
655 concurrently, excitation wavelength was set at 830 nm and a 565 nm emission dichroic was used in
656 conjunction with green (500-550 nm) and red (584-676 nm) filters for fluorescence emission detection
657 on separate photomultiplier tubes.

658 *Imaging of microglia and brain structures*
659 When imaging microglia (Alexa 594 conjugated IB4-isolectin) and brain structures (CellTracker Green
660 BODIPY), imaging was done separately. Imaging of Alexa 594 was first done with excitation wavelength
661 set to 810 nm and fluorescence emission detection through the red filter. Subsequently, imaging of
662 CellTracker Green BODIPY was performed at excitation wavelength 710 nm and the fluorescence
663 emission detected through the green filter.

664 *Imaging of axons*
665 When imaging RGC axons only (pHtdGFP), excitation wavelength was set to 910 nm and fluorescence
666 emission detected through the green filter.

667 <u>2-photon laser-induced injury</u>

668 Laser irradiation injury was carried out by focusing the 2-photon laser beam to a location within the
669 tectal neuropil. The 2-photon laser was scanned repeatedly over an approximately 10x10 µm region
670 under high laser power at wavelength 710 nm for approximately 10 seconds.

671 <u>Microglial depletion</u>

672 PLX5622 was dissolved in DMSO at 20 mM, aliquoted, and stored at -20°C. Thawed aliquots of PLX5622
673 were sonicated briefly for 1 minute before dilution in PEG 400. PEG400 solution was then further diluted
674 in a solution of 0.1X MBSH containing non-ionic surfactants poloxamer 407 and D-α-tocopherol
675 polyethylene glycol 1000 succinate to form a mixed micelle drug delivery vehicle (Guo et al., 2013). Final
676 vehicle rearing solution consisted of 2.5% polyethylene glycol 400, 0.08% poloxamer 407, 0.02% D-α-
677 tocopherol polyethylene glycol 1000 succinate, and 0.05% DMSO in 0.1X MBSH.

678 Initially, animals were reared in 0.1X MBSH. At stage 35-40, animals were transferred to vehicle rearing
679 solution with or without 10 µM PLX5622 for rearing. Rearing solutions were refreshed daily with newly
680 prepared drug and vehicle solutions.

681 Microscopy image processing and analysis

682 *Real-time imaging*
683 Microglia were labeled with Alexa 594 conjugated IB4-isolectin and axons were labeled with eGFP or
684 pHtdGFP. The red (microglia) channel was denoised with the 3D hybrid median filter plugin, and the
685 green (axon) channel was non-local means-denoised with CANDLE (Coupé et al., 2012). Time series were
686 registered by descriptor based series registration (Preibisch et al., 2010). For real-time trogocytosis
687 experiments, microglia 3D region of interests (ROIs) were generated using the 3D object counter plugin
688 (Bolte and Cordelières, 2006). Green fluorescence intensity within microglia 3D ROIs was measured
689 using the 3D ROI manager plugin (Ollion et al., 2013). Movies were generated using Imaris software or
690 ImageJ. For microglial mobility experiments, manual tracking of microglia was carried out using the
691 TrackMate plugin (Tinevez et al., 2017).

692 *Trogocytosis assay*
693 In stage 39/40 animals, microglia were labeled with Alexa 594 conjugated IB4-isolectin and axons were
694 labeled with plasmids encoding pHtdGFP or SYP-pHtdGFP. The optic tectum was imaged on day 4 (stage
695 46) and day 5 (stage 47) post-electroporation. Laser power and photomultiplier tube voltage was kept
696 constant on both days, and 150 µm thick z-stacks at 1 µm intervals were captured. The number of axons
697 was counted manually. Data was excluded if apoptotic bodies were detected, or if the number of
698 labeled axons fell from day 4 to day 5. An automated ImageJ macro script was used to calculate the
699 average microglial green fluorescence within the z-stack. The mode of the green (axon) channel was
700 calculated and subtracted for background removal. Microglia 3D ROIs were generated using the 3D
701 object counter plugin (Bolte and Cordelières, 2006). To automatically segmentate microglia, the mean
702 voxel intensity and standard deviation were calculated for the z-stack of the red channel. The 3D object
703 counter threshold was set to be the mean red value plus 2 standard deviations. A minimum threshold
704 size of 1500 voxels was used to exclude background voxels from analysis. The 3D ROI manager plugin
705 (Ollion et al., 2013) was then used to measure the green fluorescence density of each microglial cell
706 within the z-stack. Non-microglial ROIs such as melanophores were excluded, as well as microglia which
707 had overlapping voxels with the axon, and the average microglial green fluorescence density for the
708 microglia population in the z-stack was determined.

709 *Microglia quantification*
710 At stage 39/40, microglia were labeled by icv injection of Alexa 594-conjugated IB4-isolectin and brain
711 structures were labeled by icv injection with CellTracker Green BODIPY. 150 µm thick z-stacks of the
712 optic tectum at 1 µm intervals were collected daily on days 2–5 after the start of treatment. The number
713 of microglia within the optic tectum and microglia process numbers were manually counted by an
714 experimenter blind to treatment group.

715 *Axon morphology analysis*
716 Single RGC neurons were transfected with plasmid DNA as described above. 2-photon z-stacks were
717 captured daily from 2 to 5 days post-electroporation. Z-stacks were denoised with CANDLE (Coupé et al.,
718 2012), and were manually traced using Imaris 6 software by an experimenter blind to treatment group.
719 For visualization purposes, the 3D object counter (Bolte and Cordelières, 2006) and 3D ROI manager
720 (Ollion et al., 2013) plugins were used on z-stacks to segment and efface melanophores on the dorsal
721 dermal surface of the animal before maximum intensity projection.

722 *Colocalization analysis*
723 Single RGC neurons were electroporated with a plasmid encoding aRCA3-mCherry-P2A-SYP-pHtdGFP. 2-
724 photon z-stacks were captured on day 3 post-electroporation. aRCA3-mCherry (red) and SYP-pHtdGFP
725 (green) channels were captured concurrently at wavelength 990 nm. Red and green channels were
726 denoised using the 3D hybrid median filter ImageJ plugin. A 3D mask of the axon was generated by
727 summing the red and green channels and using an intensity threshold to segment the axon. Pearson's
728 correlation coefficient (Manders et al., 1993) of the masked axon was calculated using Imaris software,
729 with thresholds determined automatically using the method of Costes (Costes et al., 2004).

730 Looming Stimulus Behavioral Assay

731 *Experimental setup*
732 Stage 47 tadpoles (vehicle control or microglia-depleted) were placed within a closed 60 mm petri dish
733 and allowed to swim freely. The petri dish was placed on the bottom of a large shallow (20 cm diameter,
734 8 cm deep) glass culture dish filled completely with 0.1X MBSH. The large shallow glass culture dish was
735 placed on a purple 3D printed stage to allow for automated segmentation of albino tadpoles which are
736 predominately white and yellow colored. A webcam was placed above the tadpole to record tadpole
737 behavior, while a 2000 lumens projector customized by 3D printing to shorten the focal distance, was
738 used to project visual stimuli onto a white piece of paper taped to the side of the large glass culture
739 dish. Glare from ceiling lights was removed from webcam recordings by hanging a large black umbrella
740 over the setup.

741 *Stimulus presentation and recording*
742 Dark or bright looming stimuli were presented using custom code written in Python 3. An expanding
743 circle was drawn on the projector screen (800x600 pixels or 10.6x8 cm) using the PsychoPy library
744 (Peirce et al., 2019). For dark looming stimuli, a black (29 cd/m^2) expanding circle was drawn over a
745 white (208 cd/m^2) background. For bright looming stimuli, a white (208 cd/m^2) expanding circle was
746 drawn over a black (29 cd/m^2) background. During looming, the size of the circle expanded exponentially
747 at 10% per frame at 60 frames per second, from a diameter of 54 pixels (7 mm) until it encompassed the
748 entire screen 0.5 s later. After another 0.8 s, the screen was reset and a 10 s refractory period
749 commenced. In parallel to stimulus presentation, 480p video was recorded by webcam using the
750 OpenCV library (Bradski, 2000). Ten looming stimulus trials per animal were recorded.

751 *Automated tracking of tadpole behavior*
752 Custom computer vision tadpole tracking code was written using Python 3 and OpenCV (Bradski, 2000).
753 Feature detection on the petri dish was used to automatically determine the scale of video data.
754 Background was subtracted and thresholding was utilized to segmentate the tadpole, and the resulting
755 mask was fit to an ellipse to extract location and speed, as well as directional data and escape angle.
756 Location data from 0 – 2 s following the onset of the looming stimulus was summarized and displayed as
757 a contrail. Instantaneous velocity (activity) for the 3 s before and after the looming stimulus was also
758 extracted and compared by area under curve analysis.

759 *Discrimination of positive and negative responses to looming stimuli*
760 An automated python script was used to randomize tadpole videos and a user blinded to treatment
761 categorized tadpole responses to looming stimuli as defensive escape behavior (positive response),
762 absence of defensive escape behavior (negative response), or undeterminable (excluded from response
763 rate calculation). Typically, tadpole responses were categorized as undeterminable if the tadpole was

764 moving quickly when the looming stimulus was presented, making it difficult to discern whether
765 defensive behavior was elicited. The response rate was calculated as the number of positive responses
766 divided by the combined number of positive and negative responses.

767 *Assessment of motor responses*
768 Positive escape responses were further analyzed to compare motor data. Escape distance over 2
769 seconds from the onset of the loom was calculated from positional data, as well as the maximum escape
770 velocity. The initial escape angle was also measured from heading data. In dark looming stimuli trials,
771 the initial escape angle was defined as the absolute value of the change in heading from 0 – 0.6 s. For
772 bright looming stimuli trials, the initial escape angle was defined as the absolute value of the change in
773 heading from 0 – 1.2 s. The difference in measuring initial escape angle for dark and bright looming
774 stimuli is because dark looming stimuli evoked escape movement starting approximately 0.5 s after
775 looming onset, whereas responses to bright looming stimuli were more delayed and showed greater
776 variation in escape onset time, with the majority of responses having been initiated by 1.0 s.

777 Bioinformatics analysis

778 *Identification of complement inhibitory proteins*
779 To identify candidate complement inhibitory proteins, the STRING database was used to look for
780 functional interactions between complement C3 and other proteins. The STRING database assembles
781 information about known and predicted protein-protein interactions based on a number of different
782 sources and repositories (Szklarczyk et al., 2019). Human complement C3 was queried on the STRING
783 database using a medium confidence (0.4) minimum interaction score, and a limit of 10 and 20
784 interactors for the 1st and 2nd shell, respectively. Sources was limited to textmining, experiments and
785 databases. Proteins that are abundant in CCP modules were highlighted.

786 *Expression of complement inhibitory proteins in human cortical cells*
787 The Allen Brain Map Human Transcriptomics Cell Types Database (Allen Institute for Brain Science, 2015)
788 was used to examine human transcriptomics cell types for expression of candidate proteins identified
789 from the STRING query. This dataset was obtained from single-nucleus RNA-sequencing on
790 neurosurgical and postmortem human cortex tissue from six cortical regions (Hodge et al., 2019; Tasic et
791 al., 2018). Cell taxonomy and hierarchical clustering was retained from previous analysis (Hodge et al.,
792 2019). Gene expression of complement inhibitory proteins across distinct brain cell clusters was
793 examined and plotted using R software and the Bioconductor (Huber et al., 2015), ComplexHeatmap (Gu
794 et al., 2016), and ColorBrewer (Neuwirth, 2014) packages.

795 *Homology search*
796 The protein sequence of CD46 (NCBI accession #: NP_002380.3) was queried in the Xenopus laevis
797 genome with NCBI protein-protein BLAST (Altschul et al., 1990). The top hit was XP_018102062.1, a
798 predicted protein from the gene LOC108708165. Querying XP_018102062.1 in the Xenopus tropicalis
799 genome yielded the identity of the NP_001120599.1: Amphibian Regulator of Complement Activation
800 protein 3 (Oshiumi et al., 2009).

801 *Conserved modular architecture analysis*
802 The SMART protein domain research tool (Letunic and Bork, 2018; Schultz et al., 1998) was used to
803 determine and compare conserved modular architecture of human CD46 and X*enopus laevis* aRCA3.

804 *Transmembrane topology*
805 The Phobius transmembrane topology tool (Käll et al., 2004, 2007) was used to compare the
806 transmembrane topology of aRCA3 and CD46.

807 *Kinase prediction*
808 The NetPhos 3.1 tool (Blom et al., 2004) was used to make predictions of tyrosine phosphorylation sites
809 on the intracellular C-terminus of aRCA3. A cutoff score of 0.6 was used.

810 RNAscope *in situ* hybridization

811 *Tissue preparation*
812 The RNAscope (Wang et al., 2012) fixed-frozen tissue sample preparation and pretreatment protocol
813 provided by the manufacturer was modified for *Xenopus laevis* tadpoles. Stage 46 tadpoles were
814 euthanized in 0.2% MS-222 in 0.1X MBSH. Tadpoles were then fixed in 4% PFA at 4°C for 24 hours on a
815 laboratory rocker. For cryoprotection, tadpoles were then moved sequentially through 10%, 20% and
816 30% sucrose in 1X PBS, until samples sunk to the bottom of the container. Cryoprotected tadpoles were
817 then embedded in OCT blocks on dry ice. OCT blocks were sectioned at 8 µm thickness on a cryostat and
818 mounted on superfrost plus slides. To enhance tissue adhesion, slides were air dried for 2 hours at -20°C
819 and baked at 60°C for 30 minutes. Slides were then post-fixed by immersion in 4% PFA for 15 minutes,
820 and then dehydrated with 50%, 70% and 100% ethanol. Slides were treated with hydrogen peroxide to
821 block endogenous peroxidases. For target retrieval, using a hot plate and beaker, slides were boiled in
822 RNAscope target retrieval reagent and then treated with RNAscope Protease III.

823 *RNAscope assay*
824 The RNAscope Multiplex Fluorescent 2.0 Assay was performed according to manufacturer's protocols
825 using the HybEZ oven. In brief, probes were applied to slides, and 3 amplification steps were carried out.
826 Opal 570 dye was applied to slides along with DAPI counterstain. Coverslips were mounted with Prolong
827 gold antifade mountant. Slides were imaged with a Leica TCS SP8 confocal.

828 Molecular biology

829 *cDNA library*
830 Stage 40 Tadpoles were euthanized in 0.2% MS-222 in 0.1X MBSH. Animals were transferred to TRIzol
831 Reagent and homogenized by sonication and processed according to manufacturer's protocols to isolate
832 mRNA. Superscript IV reverse transcriptase was then used according to manufacturer's protocol to
833 generate whole tadpole cDNA.

834 *Cloning and plasmid isolation*
835 Cloning of *Xenopus laevis* cDNA was carried out using primers flanking genes of interest. Primers were
836 generated according to mRNA sequences for aRCA3 (XM_018246573.1), VAMP2.S (NM_001087474.1),
837 and c3.L (XM_018253729.1) predicted by NCBI (NCBI Resource Coordinators, 2018) and Xenbase (Karimi
838 et al., 2018). Synaptophysin was subcloned from a mouse fluorescent protein tagged synaptophysin
839 (Ruthazer et al., 2006). pHtdGFP was subcloned from a pFA6a plasmid (Roberts et al., 2016). PCR was
840 performed with Phusion High-Fidelity DNA polymerase and DNA fragments were cut with NEB enzymes
841 and ligated into a plasmid with an EF1α promotor, ampicillin resistance, and a P2A self-cleaving
842 construct when appropriate. DH5α bacteria were transformed and single clone colonies containing

843 inserts were isolated. Endotoxin free plasmid preparations of high yield and purity for electroporation
844 was prepared by maxi-prep.

845 *Design of fusion proteins*
846 The SYN-pHtdGFP fusion protein was created by in-frame fusion of pHtdGFP to the C-terminus of SYN
847 between a 3 amino acid linker (QGT). The aRCA3-mCherry fusion protein was created by an in-frame
848 fusion of mCherry to the C-terminus of aRCA3 between a 2 amino acid linker (AC). The VAMP2-C3 fusion
849 protein was created by an in-frame fusion of C3 to the C-terminus of VAMP2 between an 18 amino acid
850 linker (ASIKSPVQPLSAHSPVCI). The long linker for VAMP2-C3 was chosen to ensure that the C-terminus
851 transmembrane domain of VAMP2 would not sterically hinder proper folding of C3.

852 Statistical analysis

853 Statistical analysis was performed using Graphpad Prism 8 software. All data is presented as mean ±
854 SEM, unless otherwise noted.

855 *Pairwise comparisons*
856 Pairwise comparisons between two groups were tested by unpaired t-test.

857 *Group data*
858 If no datapoints were missing, 2-way repeated measures ANOVA was used to test group data unless a 3-
859 way design was appropriate. If an interaction was found, the interaction was reported and Sidak's
860 multiple comparison test was used to test between groups or time points as appropriate. If no
861 interaction was found, then the main effect was reported. Conversely, if the data contained missing
862 values (due to loss of animals during a time course), the mixed effect restricted maximum likelihood
863 model was used which is compatible with missing values. If a 3-way design was appropriate, 3-way
864 repeated measures ANOVA was carried out. Post-hoc tests comparing all means to other means were
865 corrected for multiple comparisons using the two-stage step-up method of Benjamini, Kriger, and
866 Yekutieli (Benjamini et al., 2006) with a false discovery rate of 0.05.

867 *Linear regression*
868 All regression analysis in this report was carried out with simple linear regression.

869 **Data and Code Availability**

870 The documented source code and user guide for the looming stimulus presentation and tadpole tracking
871 software module, XenLoom (Beta), developed in this study is made available at
872 https://github.com/tonykylim/XenLoom_beta.
873

874

875 **References**

876 Ahmari, S.E., Buchanan, J., and Smith, S.J. (2000). Assembly of presynaptic active zones from cytoplasmic
877 transport packets. Nat. Neurosci. *3*, 445–451.

878 Allen Institute for Brain Science (2015). Allen Cell Types Database.

879 Altschul, S.F., Gish, W., Miller, W., Myers, E.W., and Lipman, D.J. (1990). Basic local alignment search
880 tool. J. Mol. Biol. *215*, 403–410.

881 Barilla-LaBarca, M.L., Liszewski, M.K., Lambris, J.D., Hourcade, D., and Atkinson, J.P. (2002). Role of
882 membrane cofactor protein (CD46) in regulation of C4b and C3b deposited on cells. J. Immunol. Baltim.
883 Md 1950 *168*, 6298–6304.

884 Barker, A.J., and Baier, H. (2015). Sensorimotor Decision Making in the Zebrafish Tectum. Curr. Biol. *25*,
885 2804–2814.

886 Benjamini, Y., Krieger, A.M., and Yekutieli, D. (2006). Adaptive linear step-up procedures that control the
887 false discovery rate. Biometrika *93*, 491–507.

888 Blom, N., Sicheritz-Pontén, T., Gupta, R., Gammeltoft, S., and Brunak, S. (2004). Prediction of post-
889 translational glycosylation and phosphorylation of proteins from the amino acid sequence. Proteomics
890 *4*, 1633–1649.

891 Bolte, S., and Cordelières, F.P. (2006). A guided tour into subcellular colocalization analysis in light
892 microscopy. J. Microsc. *224*, 213–232.

893 Bradski, G. (2000). The OpenCV Library. Dr Dobbs J. Softw. Tools.

894 Casey, J.R., Grinstein, S., and Orlowski, J. (2010). Sensors and regulators of intracellular pH. Nat. Rev.
895 Mol. Cell Biol. *11*, 50–61.

896 Chan, C.-S., Weeber, E.J., Kurup, S., Sweatt, J.D., and Davis, R.L. (2003). Integrin Requirement for
897 Hippocampal Synaptic Plasticity and Spatial Memory. J. Neurosci. *23*, 7107–7116.

898 Costes, S.V., Daelemans, D., Cho, E.H., Dobbin, Z., Pavlakis, G., and Lockett, S. (2004). Automatic and
899 quantitative measurement of protein-protein colocalization in live cells. Biophys. J. *86*, 3993–4003.

900 Coupé, P., Munz, M., Manjón, J.V., Ruthazer, E.S., and Louis Collins, D. (2012). A CANDLE for a deeper in
901 vivo insight. Med. Image Anal. *16*, 849–864.

902 Cunningham, C.L., Martínez-Cerdeño, V., and Noctor, S.C. (2013). Microglia Regulate the Number of
903 Neural Precursor Cells in the Developing Cerebral Cortex. J. Neurosci. *33*, 4216–4233.

904 Dalmau, I., Finsen, B., Tønder, N., Zimmer, J., González, B., and Castellano, B. (1997). Development of
905 microglia in the prenatal rat hippocampus. J. Comp. Neurol. *377*, 70–84.

906 Dong, W., Lee, R.H., Xu, H., Yang, S., Pratt, K.G., Cao, V., Song, Y.-K., Nurmikko, A., and Aizenman, C.D.
907 (2009). Visual Avoidance in Xenopus Tadpoles Is Correlated With the Maturation of Visual Responses in
908 the Optic Tectum. J. Neurophysiol. *101*, 803–815.

909 Dunn, T.W., Gebhardt, C., Naumann, E.A., Riegler, C., Ahrens, M.B., Engert, F., and Del Bene, F. (2016).
910 Neural Circuits Underlying Visually Evoked Escapes in Larval Zebrafish. Neuron *89*, 613–628.

911 Elmore, M.R.P., Najafi, A.R., Koike, M.A., Dagher, N.N., Spangenberg, E.E., Rice, R.A., Kitazawa, M.,
912 Matusow, B., Nguyen, H., West, B.L., et al. (2014). Colony-stimulating factor 1 receptor signaling is
913 necessary for microglia viability, unmasking a microglia progenitor cell in the adult brain. Neuron *82*,
914 380–397.

915 Erblich, B., Zhu, L., Etgen, A.M., Dobrenis, K., and Pollard, J.W. (2011). Absence of colony stimulation
916 factor-1 receptor results in loss of microglia, disrupted brain development and olfactory deficits. PloS
917 One *6*, e26317.

918 Fotowat, H., and Gabbiani, F. (2011). Collision Detection as a Model for Sensory-Motor Integration.
919 Annu. Rev. Neurosci. *34*, 1–19.

920 Gosse, N.J., Nevin, L.M., and Baier, H. (2008). Retinotopic order in the absence of axon competition.
921 Nature *452*, 892–895.

922 Gu, Z., Eils, R., and Schlesner, M. (2016). Complex heatmaps reveal patterns and correlations in
923 multidimensional genomic data. Bioinforma. Oxf. Engl. *32*, 2847–2849.

924 Guo, Y., Luo, J., Tan, S., Otieno, B.O., and Zhang, Z. (2013). The applications of Vitamin E TPGS in drug
925 delivery. Eur. J. Pharm. Sci. *49*, 175–186.

926 Haas, K., Jensen, K., Sin, W.C., Foa, L., and Cline, H.T. (2002). Targeted electroporation in Xenopus
927 tadpoles in vivo--from single cells to the entire brain. Differ. Res. Biol. Divers. *70*, 148–154.

928 Håvik, B., Le Hellard, S., Rietschel, M., Lybæk, H., Djurovic, S., Mattheisen, M., Mühleisen, T.W.,
929 Degenhardt, F., Priebe, L., Maier, W., et al. (2011). The Complement Control-Related Genes CSMD1 and
930 CSMD2 Associate to Schizophrenia. Biol. Psychiatry *70*, 35–42.

931 Hodge, R.D., Bakken, T.E., Miller, J.A., Smith, K.A., Barkan, E.R., Graybuck, L.T., Close, J.L., Long, B.,
932 Johansen, N., Penn, O., et al. (2019). Conserved cell types with divergent features in human versus
933 mouse cortex. Nature *573*, 61–68.

934 Hoshiko, M., Arnoux, I., Avignone, E., Yamamoto, N., and Audinat, E. (2012). Deficiency of the microglial
935 receptor CX3CR1 impairs postnatal functional development of thalamocortical synapses in the barrel
936 cortex. J. Neurosci. Off. J. Soc. Neurosci. *32*, 15106–15111.

937 Huber, W., Carey, V.J., Gentleman, R., Anders, S., Carlson, M., Carvalho, B.S., Bravo, H.C., Davis, S., Gatto,
938 L., Girke, T., et al. (2015). Orchestrating high-throughput genomic analysis with Bioconductor. Nat.
939 Methods *12*, 115–121.

940 Javaherian, A., and Cline, H.T. (2005). Coordinated Motor Neuron Axon Growth and Neuromuscular
941 Synaptogenesis Are Promoted by CPG15 In Vivo. Neuron *45*, 505–512.

942 Ji, K., Akgul, G., Wollmuth, L.P., and Tsirka, S.E. (2013). Microglia actively regulate the number of
943 functional synapses. PloS One *8*, e56293.

944 Käll, L., Krogh, A., and Sonnhammer, E.L.L. (2004). A combined transmembrane topology and signal
945 peptide prediction method. J. Mol. Biol. *338*, 1027–1036.

946 Käll, L., Krogh, A., and Sonnhammer, E.L.L. (2007). Advantages of combined transmembrane topology
947 and signal peptide prediction--the Phobius web server. Nucleic Acids Res. *35*, W429-432.

948 Karimi, K., Fortriede, J.D., Lotay, V.S., Burns, K.A., Wang, D.Z., Fisher, M.E., Pells, T.J., James-Zorn, C.,
949 Wang, Y., Ponferrada, V.G., et al. (2018). Xenbase: a genomic, epigenomic and transcriptomic model
950 organism database. Nucleic Acids Res. *46*, D861–D868.

951 Khakhalin, A.S., Koren, D., Gu, J., Xu, H., and Aizenman, C.D. (2014). Excitation and inhibition in recurrent
952 networks mediate collision avoidance in Xenopus tadpoles. Eur. J. Neurosci. *40*, 2948–2962.

953 Kim, M., Haney, J.R., Zhang, P., Hernandez, L.M., Wang, L., Perez-Cano, L., and Gandal, M.J. (2020).
954 Network signature of complement component 4 variation in the human brain identifies convergent
955 molecular risk for schizophrenia (Genomics).

956 Letunic, I., and Bork, P. (2018). 20 years of the SMART protein domain annotation resource. Nucleic
957 Acids Res. *46*, D493–D496.

958 Ling, E.A., Kaur, C., Yick, T.Y., and Wong, W.C. (1990). Immunocytochemical localization of CR3
959 complement receptors with OX-42 in amoeboid microglia in postnatal rats. Anat. Embryol. (Berl.) *182*,
960 481–486.

961 Lozahic, S., Christiansen, D., Manié, S., Gerlier, D., Billard, M., Boucheix, C., and Rubinstein, E. (2000).
962 CD46 (membrane cofactor protein) associates with multiple beta1 integrins and tetraspans. Eur. J.
963 Immunol. *30*, 900–907.

964 Manders, E.M.M., Verbeek, F.J., and Aten, J.A. (1993). Measurement of co-localization of objects in dual-
965 colour confocal images. J. Microsc. *169*, 375–382.

966 Milinkeviciute, G., Henningfield, C.M., Muniak, M.A., Chokr, S.M., Green, K.N., and Cramer, K.S. (2019).
967 Microglia Regulate Pruning of Specialized Synapses in the Auditory Brainstem. Front. Neural Circuits *13*,
968 55.

969 Mitchell, A.J., Pradel, L.C., Chasson, L., Rooijen, N.V., Grau, G.E., Hunt, N.H., and Chimini, G. (2010).
970 Technical Advance: Autofluorescence as a tool for myeloid cell analysis. J. Leukoc. Biol. *88*, 597–603.

971 Münch, T.A., da Silveira, R.A., Siegert, S., Viney, T.J., Awatramani, G.B., and Roska, B. (2009). Approach
972 sensitivity in the retina processed by a multifunctional neural circuit. Nat. Neurosci. *12*, 1308–1316.

973 Nakata, T., Terada, S., and Hirokawa, N. (1998). Visualization of the dynamics of synaptic vesicle and
974 plasma membrane proteins in living axons. J. Cell Biol. *140*, 659–674.

975 NCBI Resource Coordinators (2018). Database resources of the National Center for Biotechnology
976 Information. Nucleic Acids Res. *46*, D8–D13.

977 Neugebauer, K.M., and Reichardt, L.F. (1991). Cell-surface regulation of β1-integrin activity on
978 developing retinal neurons. Nature *350*, 68–71.

979 Neuwirth, E. (2014). Package 'RColorBrewer.'

980 Newman, S.L., Becker, S., and Halme, J. (1985). Phagocytosis by receptors for C3b (CR1), iC3b (CR3), and
981 IgG (Fc) on human peritoneal macrophages. J. Leukoc. Biol. *38*, 267–278.

982 Nieuwkoop, P.D., and Faber, J. (1994). Normal table of Xenopus laevis (Daudin): a systematical and
983 chronological survey of the development from the fertilized egg till the end of metamorphosis (New
984 York: Garland Pub).

985 Nimmerjahn, A., Kirchhoff, F., and Helmchen, F. (2005). Resting microglial cells are highly dynamic
986 surveillants of brain parenchyma in vivo. Science *308*, 1314–1318.

987 Norman, D.G., Barlow, P.N., Baron, M., Day, A.J., Sim, R.B., and Campbell, I.D. (1991). Three-dimensional
988 structure of a complement control protein module in solution. J. Mol. Biol. *219*, 717–725.

989 Oliva, D., Medan, V., and Tomsic, D. (2007). Escape behavior and neuronal responses to looming stimuli
990 in the crab Chasmagnathus granulatus (Decapoda: Grapsidae). J. Exp. Biol. *210*, 865–880.

991 Ollion, J., Cochennec, J., Loll, F., Escudé, C., and Boudier, T. (2013). TANGO: a generic tool for high-
992 throughput 3D image analysis for studying nuclear organization. Bioinformatics *29*, 1840–1841.

993 Oshiumi, H., Suzuki, Y., Matsumoto, M., and Seya, T. (2009). Regulator of complement activation (RCA)
994 gene cluster in Xenopus tropicalis. Immunogenetics *61*, 371–384.

995 Pangburn, M.K., Schreiber, R.D., and Müller-Eberhard, H.J. (1981). Formation of the initial C3 convertase
996 of the alternative complement pathway. Acquisition of C3b-like activities by spontaneous hydrolysis of
997 the putative thioester in native C3. J. Exp. Med. *154*, 856–867.

998 Paolicelli, R.C., Bolasco, G., Pagani, F., Maggi, L., Scianni, M., Panzanelli, P., Giustetto, M., Ferreira, T.A.,
999 Guiducci, E., Dumas, L., et al. (2011). Synaptic Pruning by Microglia Is Necessary for Normal Brain
1000 Development. Science *333*, 1456–1458.

1001 Parkhurst, C.N., Yang, G., Ninan, I., Savas, J.N., Yates, J.R., Lafaille, J.J., Hempstead, B.L., Littman, D.R.,
1002 and Gan, W.-B. (2013). Microglia promote learning-dependent synapse formation through brain-derived
1003 neurotrophic factor. Cell *155*, 1596–1609.

1004 Peirce, J., Gray, J.R., Simpson, S., MacAskill, M., Höchenberger, R., Sogo, H., Kastman, E., and Lindeløv,
1005 J.K. (2019). PsychoPy2: Experiments in behavior made easy. Behav. Res. Methods *51*, 195–203.

1006 Perry, V.H., and O'Connor, V. (2008). C1q: the perfect complement for a synaptic feast? Nat. Rev.
1007 Neurosci. *9*, 807–811.

1008 Pont-Lezica, L., Beumer, W., Colasse, S., Drexhage, H., Versnel, M., and Bessis, A. (2014). Microglia shape
1009 corpus callosum axon tract fasciculation: functional impact of prenatal inflammation. Eur. J. Neurosci.
1010 *39*, 1551–1557.

1011 Preibisch, S., Saalfeld, S., Schindelin, J., and Tomancak, P. (2010). Software for bead-based registration of
1012 selective plane illumination microscopy data. Nat. Methods *7*, 418–419.

1013 R Core Team (2018). R: A Language and Environment for Statistical Computing (Vienna, Austria: R
1014 Foundation for Statistical Computing).

1015 Riccomagno, M.M., and Kolodkin, A.L. (2015). Sculpting Neural Circuits by Axon and Dendrite Pruning.
1016 Annu. Rev. Cell Dev. Biol. *31*, 779–805.

1017 Riley-Vargas, R.C., Gill, D.B., Kemper, C., Liszewski, M.K., and Atkinson, J.P. (2004). CD46: expanding
1018 beyond complement regulation. Trends Immunol. *25*, 496–503.

1019 Ripke, S., Neale, B.M., Corvin, A., Walters, J.T.R., Farh, K.-H., Holmans, P.A., Lee, P., Bulik-Sullivan, B.,
1020 Collier, D.A., Huang, H., et al. (2014). Biological insights from 108 schizophrenia-associated genetic loci.
1021 Nature *511*, 421–427.

1022 Roberts, T.M., Rudolf, F., Meyer, A., Pellaux, R., Whitehead, E., Panke, S., and Held, M. (2016).
1023 Identification and Characterisation of a pH-stable GFP. Sci. Rep. *6*, 1–9.

1024 Robles, E., Laurell, E., and Baier, H. (2014). The Retinal Projectome Reveals Brain-Area-Specific Visual
1025 Representations Generated by Ganglion Cell Diversity. Curr. Biol. *24*, 2085–2096.

1026 Ruthazer, E.S., Akerman, C.J., and Cline, H.T. (2003). Control of axon branch dynamics by correlated
1027 activity in vivo. Science *301*, 66–70.

1028 Ruthazer, E.S., Li, J., and Cline, H.T. (2006). Stabilization of Axon Branch Dynamics by Synaptic
1029 Maturation. J. Neurosci. *26*, 3594–3603.

1030 Ruthazer, E.S., Schohl, A., Schwartz, N., Tavakoli, A., Tremblay, M., and Cline, H.T. (2013a). Bulk
1031 Electroporation of Retinal Ganglion Cells in Live Xenopus Tadpoles. Cold Spring Harb. Protoc. *2013*,
1032 pdb.prot076471.

1033 Ruthazer, E.S., Schohl, A., Schwartz, N., Tavakoli, A., Tremblay, M., and Cline, H.T. (2013b). In Vivo Time-
1034 Lapse Imaging of Neuronal Development in Xenopus. Cold Spring Harb. Protoc. *2013*, pdb.top077156.

1035 Sahu, A., Kozel, T.R., and Pangburn, M.K. (1994). Specificity of the thioester-containing reactive site of
1036 human C3 and its significance to complement activation. Biochem. J. *302*, 429–436.

1037 Sankaranarayanan, S., and Ryan, T.A. (2000). Real-time measurements of vesicle-SNARE recycling in
1038 synapses of the central nervous system. Nat. Cell Biol. *2*, 197–204.

1039 Schafer, D.P., Lehrman, E.K., Kautzman, A.G., Koyama, R., Mardinly, A.R., Yamasaki, R., Ransohoff, R.M.,
1040 Greenberg, M.E., Barres, B.A., and Stevens, B. (2012). Microglia Sculpt Postnatal Neural Circuits in an
1041 Activity and Complement-Dependent Manner. Neuron *74*, 691–705.

1042 Schindelin, J., Arganda-Carreras, I., Frise, E., Kaynig, V., Longair, M., Pietzsch, T., Preibisch, S., Rueden, C.,
1043 Saalfeld, S., Schmid, B., et al. (2012). Fiji: an open-source platform for biological-image analysis. Nat.
1044 Methods *9*, 676–682.

1045 Schultz, J., Milpetz, F., Bork, P., and Ponting, C.P. (1998). SMART, a simple modular architecture research
1046 tool: Identification of signaling domains. Proc. Natl. Acad. Sci. *95*, 5857–5864.

1047 Sellgren CM, Gracias J, Watmuff B, Biag JD, Thanos JM, Whittredge PB, Fu T, Worringer K, Brown HE,
1048 Wang J, et al. (2019). Increased synapse elimination by microglia in schizophrenia patient-derived
1049 models of synaptic pruning. Nat. Neurosci. *22*, 374–385.

1050 Shinoda, H., Shannon, M., and Nagai, T. (2018). Fluorescent Proteins for Investigating Biological Events in
1051 Acidic Environments. Int. J. Mol. Sci. *19*.

1052 Smolders, S.M.-T., Swinnen, N., Kessels, S., Arnauts, K., Smolders, S., Bras, B.L., Rigo, J.-M., Legendre, P.,
1053 and Brône, B. (2017). Age-specific function of α5β1 integrin in microglial migration during early
1054 colonization of the developing mouse cortex. Glia *65*, 1072–1088.

1055 Solek, C.M., Farooqi, N., Verly, M., Lim, T.K., and Ruthazer, E.S. (2018). Maternal immune activation in
1056 neurodevelopmental disorders. Dev. Dyn. *247*, 588–619.

1057 Squarzoni, P., Oller, G., Hoeffel, G., Pont-Lezica, L., Rostaing, P., Low, D., Bessis, A., Ginhoux, F., and
1058 Garel, S. (2014). Microglia Modulate Wiring of the Embryonic Forebrain. Cell Rep. *8*, 1271–1279.

1059 Stephan, A.H., Barres, B.A., and Stevens, B. (2012). The Complement System: An Unexpected Role in
1060 Synaptic Pruning During Development and Disease. Annu. Rev. Neurosci. *35*, 369–389.

1061 Stevens, B., Allen, N.J., Vazquez, L.E., Howell, G.R., Christopherson, K.S., Nouri, N., Micheva, K.D.,
1062 Mehalow, A.K., Huberman, A.D., Stafford, B., et al. (2007). The classical complement cascade mediates
1063 CNS synapse elimination. Cell *131*, 1164–1178.

1064 Svahn, A.J., Graeber, M.B., Ellett, F., Lieschke, G.J., Rinkwitz, S., Bennett, M.R., and Becker, T.S. (2013).
1065 Development of ramified microglia from early macrophages in the zebrafish optic tectum. Dev.
1066 Neurobiol. *73*, 60–71.

1067 Szklarczyk, D., Gable, A.L., Lyon, D., Junge, A., Wyder, S., Huerta-Cepas, J., Simonovic, M., Doncheva,
1068 N.T., Morris, J.H., Bork, P., et al. (2019). STRING v11: protein-protein association networks with
1069 increased coverage, supporting functional discovery in genome-wide experimental datasets. Nucleic
1070 Acids Res. *47*, D607–D613.

1071 Tasic, B., Yao, Z., Graybuck, L.T., Smith, K.A., Nguyen, T.N., Bertagnolli, D., Goldy, J., Garren, E., Economo,
1072 M.N., Viswanathan, S., et al. (2018). Shared and distinct transcriptomic cell types across neocortical
1073 areas. Nature *563*, 72–78.

1074 Temizer, I., Donovan, J.C., Baier, H., and Semmelhack, J.L. (2015). A Visual Pathway for Looming-Evoked
1075 Escape in Larval Zebrafish. Curr. Biol. *25*, 1823–1834.

1076 Tinevez, J.-Y., Perry, N., Schindelin, J., Hoopes, G.M., Reynolds, G.D., Laplantine, E., Bednarek, S.Y.,
1077 Shorte, S.L., and Eliceiri, K.W. (2017). TrackMate: An open and extensible platform for single-particle
1078 tracking. Methods *115*, 80–90.

1079 Tremblay, M.-È., Lowery, R.L., and Majewska, A.K. (2010). Microglial interactions with synapses are
1080 modulated by visual experience. PLoS Biol. *8*, e1000527.

1081 Valtorta, F., Pennuto, M., Bonanomi, D., and Benfenati, F. (2004). Synaptophysin: leading actor or walk-
1082 on role in synaptic vesicle exocytosis? BioEssays News Rev. Mol. Cell. Dev. Biol. *26*, 445–453.

1083 Wake, H., Moorhouse, A.J., Jinno, S., Kohsaka, S., and Nabekura, J. (2009). Resting microglia directly
1084 monitor the functional state of synapses in vivo and determine the fate of ischemic terminals. J.
1085 Neurosci. Off. J. Soc. Neurosci. *29*, 3974–3980.

1086 Wallace, J., Lord, J., Dissing-Olesen, L., Stevens, B., and Murthy, V.N. (2020). Microglial depletion
1087 disrupts normal functional development of adult-born neurons in the olfactory bulb. ELife *9*, e50531.

1088 Wang, C., Yue, H., Hu, Z., Shen, Y., Ma, J., Li, J., Wang, X.-D., Wang, L., Sun, B., Shi, P., et al. (2020).
1089 Microglia mediate forgetting via complement-dependent synaptic elimination. Science *367*, 688–694.

1090 Wang, F., Flanagan, J., Su, N., Wang, L.-C., Bui, S., Nielson, A., Wu, X., Vo, H.-T., Ma, X.-J., and Luo, Y.
1091 (2012). RNAscope: a novel in situ RNA analysis platform for formalin-fixed, paraffin-embedded tissues. J.
1092 Mol. Diagn. JMD *14*, 22–29.

1093 Weinhard, L., di Bartolomei, G., Bolasco, G., Machado, P., Schieber, N.L., Neniskyte, U., Exiga, M.,
1094 Vadisiute, A., Raggioli, A., Schertel, A., et al. (2018). Microglia remodel synapses by presynaptic
1095 trogocytosis and spine head filopodia induction. Nat. Commun. *9*, 1228.

1096 Werneburg, S., Jung, J., Kunjamma, R.B., Ha, S.-K., Luciano, N.J., Willis, C.M., Gao, G., Biscola, N.P.,
1097 Havton, Leif.A., Crocker, S.J., et al. (2020). Targeted Complement Inhibition at Synapses Prevents
1098 Microglial Synaptic Engulfment and Synapse Loss in Demyelinating Disease. Immunity *52*, 167-182.e7.

1099 Yilmaz, M., and Meister, M. (2013). Rapid innate defensive responses of mice to looming visual stimuli.
1100 Curr. Biol. CB *23*, 2011–2015.

1101 Zeitvogel, F., Schmid, G., Hao, L., Ingino, P., and Obst, M. (2016). ScatterJ: An ImageJ plugin for the
1102 evaluation of analytical microscopy datasets. J. Microsc. *261*, 148–156.

1103
1104

1105 **Highlights and eTOC Blurb**

1106 - Microglia trogocytose axons *in vivo*
1107 - Microglia depletion alters the behavioral responses to visual looming stimuli
1108 - Axonal arborization is enhanced by microglial depletion or overexpression of aRCA3
1109 - Axonal arborization is reduced by expression of VAMP2-C3

1110